UNIVERSITY OF BIRMINGHAM

Nanocarbon-Hydride Composites for Hydrogen Storage

Joshua Edwin Vines

A Thesis Submitted to the School of Metallurgy and Materials for the Degree of Master of Research

School of Metallurgy and Materials
University of Birmingham
Birmingham
B15 2TT,

United Kingdom

September 2012

Abstract

Graphite and $LiBH_4$ are considered possible materials for solid state hydrogen storage. The aim of this thesis was to investigate the use of a milled graphite+$LiBH_4$ composite as a potential hydrogen storage medium. The catalytic effects of milled graphite up on $LiBH_4$ were investigated, results also indicated the composite's potential for reversibility. Graphite was ball-milled for 8 h under 3 bar H_2, followed by the addition of $LiBH_4$ at a molar ratio of 2:1 (graphite:$LiBH_4$) and milled for a further 2 h. Characterization of the as milled material showed the formation of a nanocrystalline/amorphous mixture of graphite and $LiBH_4$.

Decomposition was performed by heating to 500 °C at 2 °Cmin^{-1}. Graphite milled for 8 h released a small amount of hydrogen at 350 °C, though no reaction was observed using DSC. The graphite+$LiBH_4$ sample exhibited 4 endothermic peaks consistent with a modified $LiBH_4$ decomposition; however H_2 desorption was reduced by 150 °C with no CH_4 or B_2H_6 being detected. The application of an over pressure of hydrogen during heating of the graphite+$LiBH_4$ was found to suppress the decomposition of $LiBH_4$.

In-situ XRD measurements indicated that no lattice expansion occurred during heating until 275 °C when expansion became rapid; indicating that the presence of $LiBH_4$ opposes linear lattice expansion until it melts. XRD measurements also demonstrated that Li_2C_2 was formed; Li_2C_2 is known to be a key decomposition product in making a graphite based system reversible. It was not possible to identify the exact decomposition path due to partial oxidation of the sample during the measurement.

Partial reversibility was observed at non optimized conditions of 500 °C under 100 bar H_2 for 20 min thus indicating the composite's potential for use as a reversible storage media.

The decrease in desorption temperatures of the sample coupled with the composite's potential for reversible hydrogen cycling are promising qualities. However, even lower desorption and absorption temperatures are required before the composite can be considered a possible candidate as an on-board storage medium.

Acknowledgements

I would like to thank all members of the Hydrogen Storage Materials Research Group at the University of Birmingham including my fellow research students for their help with equipment during my Project.

A special thank you must be extended to Dr Daniel Reed for all of his advice and assistance with both my project and thesis writing.

I would also like to thank my supervisor Dr David Book, for his continued input and guidance during my project.

Table of Contents

1 Introduction

As fossil fuel supplies continue to diminish and the level of CO_2 released into the atmosphere continues to rise, there is a need to find sustainable, cost-effective alternatives for the supply of energy. Hydrogen is the most abundant element on the planet and consequently can be considered as one of the most promising energy vectors in the development of a clean and sustainable energy source and fuel. Some of this potential is down to the very high energy per unit mass of hydrogen (142 $MJkg^{-1}$); 3 times greater than that associated with liquid hydrocarbon fuels 47 $MJkg^{-1}$[1]. However, particularly for mobile applications, a significant problem associated with its use is storage; its energy per unit volume is ten times smaller than that of petrol. As a result, the US Department of Energy (DoE) has set a number of targets, to be met by 2017, for an on-board hydrogen storage system for fuel cell vehicles: gravimetric capacity of 5.5 wt% H_2, volumetric capacity of 40 gL^{-1}, and a refuel rate of 1.5 kg of H_2 per minute [2]. In simple terms, 6 kg of H_2 needs to be stored on a fuel cell vehicle, in order to achieve the required range of 500 km for a modern car [3].

Currently, the limiting factor in the conversion to a H_2 economy for mobile applications is the inability to efficiently and effectively store H_2. The aim of this thesis is to investigate the potential of a ball-milled graphite+$LiBH_4$ composite to meet the above DoE targets and offer an economically viable storage medium.

2 Literature Review

2.1.Hydrogen Production Techniques

Currently 90% of global H_2 is produced via Steam Reforming [4]; it is a technique which has been used for decades and consequently has been a well refined and a commercially viable option for hydrogen production. Methane, coal gas and biomass can all be used as sources. however. as the global energy demand increases at 5%Pa and 86% of global energy is produced using fossil fuels [5] coupled with limited fossil fuel deposits, these hydrogen production techniques are not sustainable. Steam reforming techniques produce significant amounts of the Green House Gas, CO_2, as both a by-product of the reaction and from the production of the high temperatures required for the process (in excess of 900 °C).

Water can be split thermally by heating it up to temperatures in excess of 2000 °C. A rapidly recombining mixture of H_2 and O_2 is produced making separation difficult; there have been investigations into the use of thermal chemical cycles for the production of H_2 which lower splitting temperatures and can be incorporated into the designs of the latest nuclear reactors.

Electrolysis is the electrochemical splitting of water into O_2 and H_2 and may hold the key to a clean hydrogen production; the reaction process is displayed below.

Cathode: $H_2O \rightarrow H^+ + OH^-$

Anode: $OH^- \rightarrow O_2 + 2\,H_2O + 4e^-$

Overall: $2H_2O \rightarrow O_2 + 2H_2 \quad (\Delta H = -578\ kJmol^{-1})$

The water molecules are split into positive hydrogen ions H^+ (attracted to the cathode) and negative hydroxide ions OH^- (attracted to the anode). Electrons from the cathode combine with the positive hydrogen ions to form hydrogen molecules and the electrons from the negatively charged hydroxide ions transfer to the anode to complete the circuit. This reverse of this process is used in Proton Exchange Membrane (PEM) fuel cells. The gases produced as a by-product of electrolysis are pure H_2 and O_2 and as a result removes the need for gas purification processes such as Pressure Swing Absorption (PSA) and the use of membranes, however, as the reaction is endothermic it needs to be to be electrically driven.

In order keep electrolysis a zero CO_2 emission hydrogen production process, the energy used to drive the reaction should be sourced from renewable energy sources such as wind, solar or geothermal.

Although water electrolysis is the cleanest mechanism for hydrogen production, currently only 4% of the global H_2 production is generated this way [6]; further advances need to be made to increase the efficiency and reduce the cost.

2.2.Hydrogen as an On-board Fuel

Hydrogen gas can be used as a fuel for on-board applications in two ways; internal combustion or electrochemical reaction.

Hydrogen can be internally combusted with air just like petrol converting chemical energy into mechanical; however the efficiency of the process is limited by the Carnot cycle to 25% [1], slightly higher than that associated with petrol. If the air mixture is rich in O_2 then the major by-product of the reaction is water; a clean reaction process. However if the air is rich in nitrogen, then nitrogen oxides can form.

Electrochemical reaction of hydrogen with air is an entirely clean process; hydrogen reacts with the air to produce electricity and heat. The current is a result of electron transfer from oxygen to hydrogen. As the reaction is not thermal, it is not limited by the Carnot cycle allowing efficiencies of up to 60% to be achieved [1]; over twice that associated with internal combustion. The reaction between hydrogen and oxygen takes place inside of fuel cells of which there are 6 main types; Proton Exchange Membrane (PEM), Alkaline Fuel Cell (AFC), Direct Methanol Fuel Cell (DMFC), Phosphoric Acid Fuel Cell (PAFC), Molten Carbonate Fuel Cell (MCFC) and Solid Oxide Fuel Cell (SOFC). The most promising of these cells for on-board vehicular applications is the PEM fuel cell due not only to its low operating temperatures (~80 °C) but also the fact that the only products from the reaction are water and heat; Figure 2.1 demonstrates the mechanism behind the fuel cell's operation. PEM fuels cells use the same reaction as used in electrolysis, hence the technology is well established.

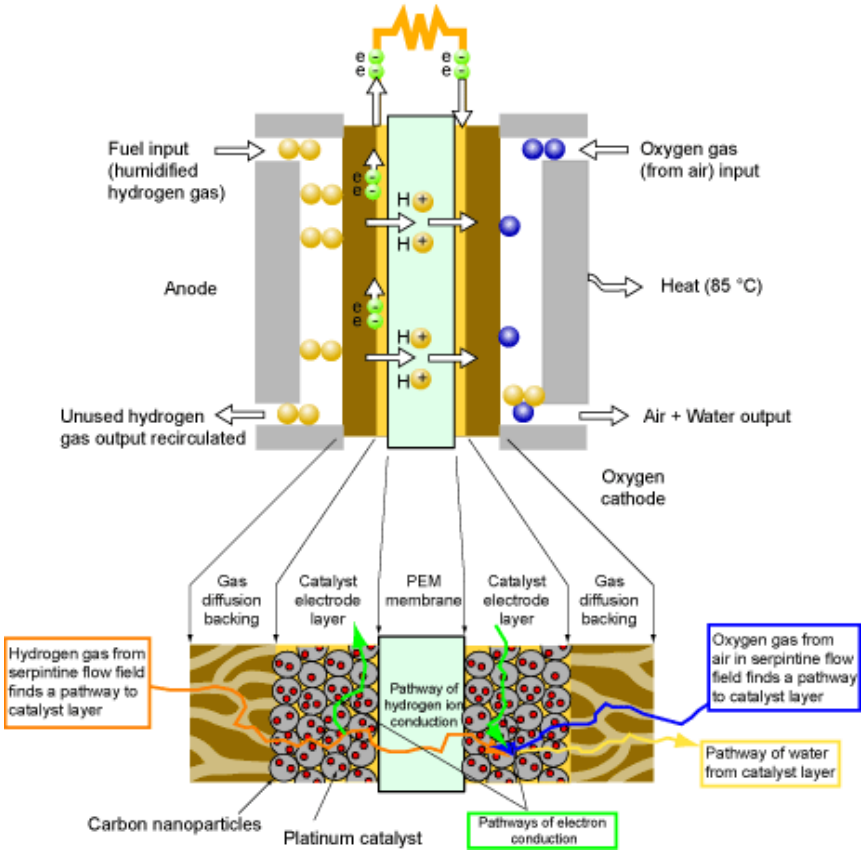

Figure 2.1. Diagram of a PEM fuel cell, showing the reaction processes [6]

Currently the largest constraint on hydrogen fuel cell cars is not the fuel cells themselves, but the hydrogen storage mechanisms used in conjunction with them; vast advances in solid state storage mechanisms are required in order to make H_2 powered cars a realistic future.

2.3. Review of Current Hydrogen Storage Techniques

2.3.1. An Ideal Storage Material

An ideal storage material would fulfil the following important criteria:

1. The material would be able to reversibly store hydrogen gas with zero degradation over cycling
2. The material would desorb and adsorb hydrogen at low, practical temperatures and pressures
3. The material would have fast kinetics allowing for fast refuelling times equivalent to refuelling times for petrol cars
4. The material would be able to store equivalent or higher gravimetric and volumetric quantities of fuel (hydrogen) than conventional petrol tanks
5. The material would be both cheap and in high abundance in order to keep fuel costs low and competitive with petrol
6. The material would desorb high purity H_2 preserving the car's fuel cell

No material has yet been found that can satisfy all the above criteria to be considered commercially viable. Current storage techniques are discussed and evaluated in this chapter.

2.3.2. Gaseous Storage of Hydrogen

Compressed gas storage of hydrogen is currently the most common way of storing hydrogen, however, conventional steel cylinders filled to pressures around 200 bar result in poor gravimetric densities. In order to store 4 kg of H_2 (the target set by the DoE as mentioned in Section 1), 5 conventional steel cylinders would be required. This type of storage is suitable for heavier vehicles and public transport where weight is not an issue, routes are predetermined and refuelling is regular. For most on-board vehicle storage applications this is not a practical solution [1]. New lightweight composite cylinders can withstand pressures up to 700 bar, however the volumetric densities are still not high enough to currently make it a viable option for future on-board hydrogen storage.

Spherical containers are structurally stronger and hence are able to hold higher pressures; a sphere 60 cm in diameter would be able to hold the 4 kg of H_2 required for a 400 km vehicle range [1]. The biggest issue with spherical containers is their fabrication coupled with their difficulty to transport and store; conventional cylinders are much cheaper to store and transport.

2.3.3. Liquid Storage of Hydrogen

The condensation of hydrogen gas into liquid greatly increases its density to 70.99 g/L [7] thus increasing the gravimetric storage density of the tank. In order to achieve this liquid state, hydrogen must be cooled under pressure to below its boiling point of -252.87 °C. It is then stored at a temperature of -251.95 °C in cryogenic tanks [8]. The boil off rate of liquid hydrogen is proportional to the surface to volume ratio; the larger the volume of the storage tank, the lower the boil off rate. As a result, although liquid storage can be practical for large scale H_2 storage, it is not seen as a suitable solution for vehicular applications due to the high

amount of energy required for liquefaction, and the boil-off experienced with this type of storage.

2.3.4. Solid State Storage of Hydrogen

A wide range of solid state storage materials have been developed which store hydrogen using different mechanisms such as physisorption and chemisorption. An ideal storage material will have both a high volumetric and gravimetric hydrogen density as well as being able to absorb and desorb hydrogen at ambient temperatures and pressures; this material would be located in the top right of Figure 2.2.

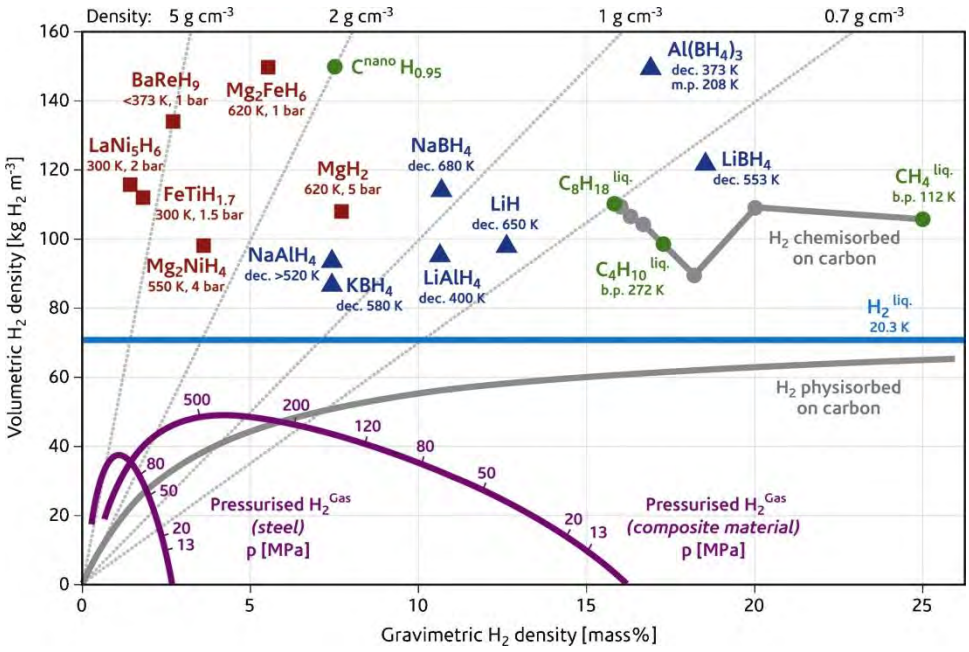

Figure 2.2. Volumetric vs. gravimetric hydrogen densities of selected hydrides [9]

Materials with large surface areas, for example single walled carbon nanotubes (SWNTs) and activated carbon, are prime candidates for physisorption, and under the correct pressure and temperature conditions (-196 °C) offer fully reversibly hydrogen cycling [8]. However, their

low operating temperatures [10] and limited gravimetric and volumetric H_2 storage densities currently make them less promising for on-board applications.

Some metal hydrides, for example $LaNi_5$, can operate at room temperature under atmospheric pressure making them a prime candidate for use as a storage media, although such materials have gravimetric densities of only ≈ 2 wt% which are not sufficient for generic on-board applications, they are suitable for niche applications where more weight is a bonus opposed to a disadvantage; for example powering forklift trucks where weight is required as ballast. These materials are located on the upper left hand side of Figure 2.2.

Complex hydrides have a hydrogen-to-metal ratio of at least 2 and are ionic or covalent compounds [8]. Their high gravimetric hydrogen densities have resulted in them being subject to significant amounts of research; $LiBH_4$ is able to store 18 wt% of H_2 at room temperature. Further discussion about $LiBH_4$ decomposition pathways are discussed in Section 2.6.2. The biggest challenges associated with complex hydrides are decomposition temperatures and reversibility, as recombination with hydrogen can be a slow process which has to be carried out under high pressure and temperature conditions [11].

Figure 2.3 shows how the volumetric size of containers able to store the DoE target of 4 kg of hydrogen compare for the different storage methods above, where Mg_2NiH_4 and $LaNi_5H_6$ are examples of solid state storage materials.

2.4. Hydrogen Bonding Processes

Ever since Dillon et al. [12] documented the potential of SWNTs in 1997 for use as a hydrogen storage medium, a wide range of carbon based materials have been researched (i.e. milled graphite, activated carbon, mesoporous carbon and carbon nanotubes) and although there is a vast array, there are two processes which can be used to characterise their C-H interactions; physisorption and chemisorption.

2.4.1. Physisorption

Physisorption is a process whereby an adsorbate is adsorbed onto the surface of a substrate; the only attraction is a result of weak Van der Waals interactions between the substrate and the sorbate. Kinetics of the process are fast as there is no activation energy required because there is no potential barrier for atoms to cross in order to physisorb; consequently low temperatures are required to store hydrogen via this process and prevent the hydrogen from desorbing back as a gas. Figure 2.4 shows a graph of distance of the adsorbate from the surface vs. energy for physisorption. When the hydrogen atoms get close enough such that their electron clouds overlap with the substrate's, the potential energy required to further decrease the distance rapidly increases.

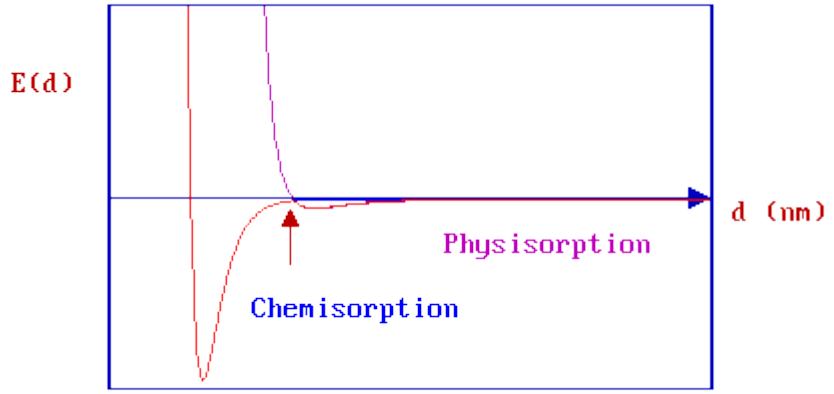

Figure 2.4. Potential Energy (E) vs. Distance of the adsorbate from the surface (d), showing the potential wells associated with physisorption and chemisorption [13]

2.4.2. Chemisorption

When hydrogen molecules approach the surface they undergo physisorption; they are then able to either desorb back into the gas or dissociate and cross the potential barrier, sharing electrons and thus bonding to the surface atoms; the latter is known as chemisorption. The kinetics of this process is dependent upon the barrier created where the two potential wells converge on the graph as indicated by the arrow displayed in Figure 2.4 and is related to the depth of the potential wells of both processes. Chemisorbed atoms are then able to pass into the subsurface layer and subsequently diffuse on the interstitial sites through the substrate [8]. In order for metal hydrides to be produced, the hydrogen molecules must first physisorb to the surface of the metal, before dissociating and chemisorbing to the surface and finally diffusing though the metal and onto interstitial sites. This concept is demonstated in Figure 2.5.

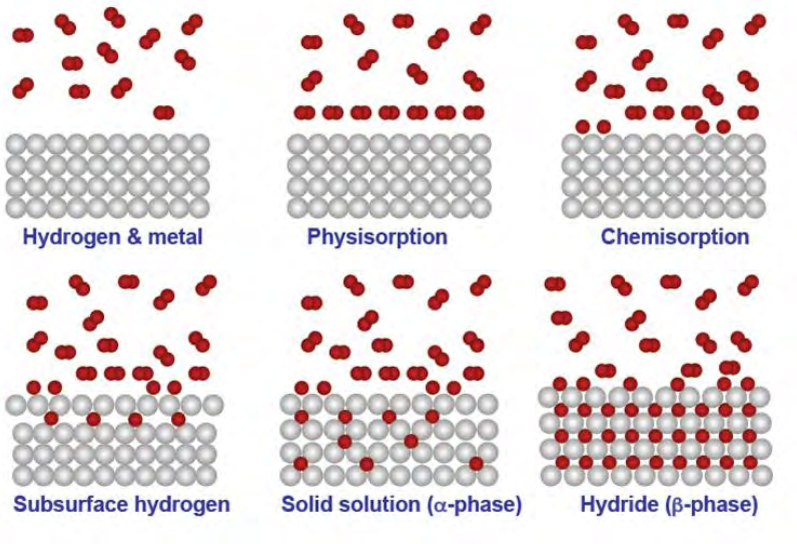

Figure 2.5. Schematic diagram displaying hydrogen absorption in metals [14]

Temperatures required for the physisorption of 5.5wt % H_2 (current DoE target) to graphite are very low (-150 °C), subsequently this process is very energy intensive. Figure 2.6 demonstrates where the current targets are in relation to different hydrogen-carbon systems. The current targets are located in the middle between the two processes. Ideal carbon based storage media will chemisorb hydrogen resulting in the formation of C-H bonds, however these bonds need to be broken during H_2 desorption hence the C-H bonds need to be destabilized in order to lower desorption temperatures whilst retaining the high storage densities that can be achieved.

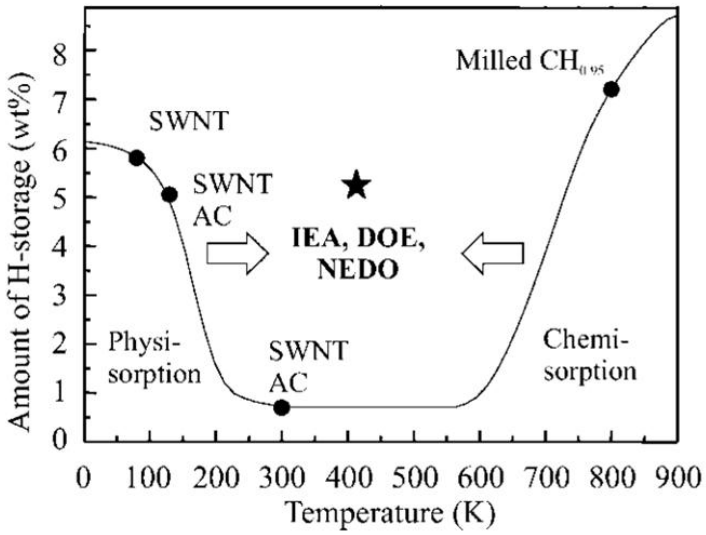

Figure 2.6. The progress of carbon-based hydrogen stores, to date, together with the targets set by the IEA, DOE, and NEDO; the regions of physisorption and chemisorption reflect the differing processes of hydrogen sorption [15, 16]

2.5. Ball-milled Graphite

2.5.1. Effects of Ball-milling on Graphite

Ball-milling is an effective process for creating nanostructured graphite suitable for hydrogen storage. When graphite is ball-milled, high impact collisions cause the graphene layers to be smashed up, resulting in deformation. Deformation of the graphene layers increases hydrogen diffusivity and creates dangling carbon bonds increasing the hydrogen storage density of the graphite [17-20].

Milling also leads to the breaking down of graphite in to a nanocrystalline and amorphous mixture. This has been shown using X-Ray Diffraction; with increased milling time the (002) diffraction peak decreases [21-24] until the graphite is completely amorphous. Raman spectroscopy has also been used to demonstrate this effect (see Section 4.2.2 for brief description of Raman spectroscopy). Asymmetric vibrations of graphite-like sp^2 bonds give rise to the G peak at 1580cm^{-1}, while symmetric vibrations of diamond-like sp^3 bonds give rise to the D peak at 1350cm^{-1}.

In perfect graphite, only the G band is present, however ball-milling induces defects causing the creation of sp^3 bonds and the presence of the D band in the Raman spectrum; the ratio of intensities of the G/D bands therefore indicates the degree of crystallinity. Increased milling times will result in a decrease in the intensity of the G peak and an increase in the intensity of the D peak as defected sp^2 bonds form sp^3 bonds [22-24].

Both the G and D peaks are a result of first order Raman processes; second order Raman processes can be seen in the spectrum of milled graphite at 1620cm-1 and 2700cm^{-1}, referred to the D′ and G′ peaks respectively. The D′ peak is associated with one elastic and one inelastic scattering event, whereas the G′ peak is attributed to two inelastic scattering events [25]. However, as both peaks are a result of the presence of the D peak they are also defect induce Raman features of graphite.

Particle size is also directly affected by milling and can be considered inversely proportion to milling time. Welham et al. [23] reported that with increased milling time, the Brunauer-Emmett-Teller (BET) surface area increased and particle size decreased. As well as being clear in SEM images, this decrease in particle size was also evident in XRD measurements; broadening of the (002) XRD peak as a result of the expected increase in strain of the new smaller particles. However after milling for 100 h, the BET surface area was calculated to decrease, this was due to the agglomeration of small particles.

2.5.2. Ball-milled Graphite for Hydrogen Storage

Ball-milled graphite has been investigated as a hydrogen storage medium, and was found to absorb up to 7.4 wt% H_2 by Orimo et al. [21] when milled under an atmosphere of 10 bar H_2 for 10 h. It was shown by Chen et al. [26] that increasing the hydrogen pressure under which milling was carried out (over the range of 3 to 60 bar), decreased the amount of H_2 absorbed; more hydrogen atoms are trapped both at the edges of the graphene sheets and between the layers which suppresses the formation of further defects. Huang et al. [27] found that using

impact mode milling gave a higher total absorption than using shearing mode milling where the gravimetric quantities absorbed were 2.7 wt% and 0.6 wt% respectively. The higher energy impact milling mode led to the creation of more defects than the low energy shearing mode, hence impact milling led to higher hydrogen absorption levels.

The optimum milling time for graphite under a 3 bar H_2 atmosphere was found to be 10 h by Zhang et al. [22]. The specific surface area of milled graphite follows the same trend, and is believed to be due to agglomeration of the graphite particles during milling [28]. Orimo et al. [21] also showed that there was significant amorphisation of the graphite after 10 h of milling. It was found that for pro-longed milling times, that hydrogen desorption quantities decreased and hydrocarbon emission increased [22, 24].

Reversible hydrogen sorption of milled graphite remains a challenge due to the high temperatures and pressures required rendering milled graphite an unpractical solution for on-board hydrogen storage. The strong covalent C-H bonds mean that temperatures in excess of 700 °C are required for the desorption of H_2, consequently research into destabilizing these bonds has become vital. The most successful attempts have using alkali metals such as lithium and potassium which form intercalated compounds with graphite [29].

During milling it is possible for the milling media to contaminate the sample and act as a catalyst reducing desorption onset temperatures and increasing gravimetric storage capacities [16, 22, 24, 27, 30]. On the other hand, these contaminants may react with the sample altering the decomposition pathway, which potentially may inhibit reversibility. Hence choice of milling media and conditions such as duration are critical if contamination is to be kept to a minimum. Zhang et al. [31] milled graphite under 3 bar H_2 using a WC milling pot and reported that no contamination was detected on samples milled for 10 h. Samples milled for

40 h displayed weak intensity XRD peaks relating to WC, along with the presence of Co identified using vibrating sample magnetometry; the Honda-Owen method was used to estimate the Co content to be 0.2 wt%.

2.6. Ball-milled Graphite with Additions

Although physisorption of hydrogen onto nanostructured carbons is a safe way of storing hydrogen (when compared to the actual and perceived risks of storing hydrogen as a liquid or under high pressures) it has been concluded that it is not the most viable option for on-board room temperature applications [32-35]. Consequently research efforts now focus on destabilizing the strong C-H covalent bonds in order to alter the thermodynamics of the reaction. Recent efforts are based up on the combination of ball-milled graphite with metallic additions in order to increase reaction kinetics and hydrogen capacity whilst reducing desorption temperatures.

2.6.1. Ball-milled Graphite with Fe Addition

Graphite-Fe combinations have been shown to hold up to 10 wt% H_2 [30, 36, 37] generating interest in to related research. Zhang and Book [31] ball-milled graphite with 0.5 wt% Fe for 10 h, upon heating to 990 °C they found that the H_2 desorption temperature was 50 °C lower (350 °C) and a total of 9.6 wt% hydrogen was released, no methane was detected. However, samples that were milled for a prolonged period of 40 h desorbed less hydrogen and also released methane. It was concluded that "the iron carbide produced during milling plays a catalytic role, increasing the hydrogen storage capacity and lowering the onset temperature of the hydrogen desorption" [31]. Ichikawa et al. [30] found that the lower desorption temperature coincided with Fe_3C crystal growth, thus also concluding that Fe_3C plays a catalytic role in hydrogen release from graphite.

2.6.2. Ball-milled Graphite with LiH Addition

Lithium hydride is widely considered to be too stable for use as a hydrogen storage medium by itself, requiring temperatures in excess of 700 °C to decompose. In 2005 Ichikawa et al. [38] demonstrated that LiH could be destabilized by close contact with LiOH or NaOH due to interactions between the LiH and polar molecules. This led them to create a Li-C-H system by ball-milling hydrogenated nanostructured graphite ($C^{nano}H_{x)}$ and LiH; their results suggested that hydrogen was desorbed below 350 °C, although heating up to 400 °C was required to ensure all H_2 was desorbed.

As a result of these findings, in 2009 Ichikawa et al. [39] were able to reversibly store 5 wt% hydrogen using a Li-C-H system over 5 cycles before the gravimetric capacity became greatly reduced. The sample consisted of $C^{nano}H_x$ milled for 80 h under a 10 bar H_2 atmosphere at room temperature which was then milled for a further 2 h with the LiH addition under the same conditions with molar ratio of 2:1 ($C^{nano}H_x$:LiH). They were able to reversibly store 5 wt% H_2 over 2 de/re-hydriding phases; after the 2nd cycle the amount of stored H_2 decreased due to production of hydrocarbons during rehydrogenation. This system is able to act reversibly due to the formation of Li_2C_2 during dehydrogenation; Equation 1 shows the decomposition of system.

$$2C^{nano}H_x + LiH \rightarrow C^{nano} + \frac{1}{2}Li_2C_2 + \left[\frac{4x+2}{4}\right]H_2 \text{ [40]}$$

Equation 1: Decomposition process of $C^{nano}H_2$ + LiH

2.7. Lithium Borohydride as a Hydrogen Storage Material

2.7.1. Lithium Borohydride Current Capabilities

The high gravimetric and volumetric hydrogen densities of lithium borohydride (18 wt% and 122 kgm^{-3} respectively) render it a promising option for solid state hydrogen storage; recent studies have found it to reversibly store hydrogen when heated to 600 °C under 350 bar H_2 [41]. Efforts have been made to try and destabilize $LiBH_4$ in order to reduce its high hydrogen desorption temperature (450 °C [42]) and improve its reversibility. The addition of MgH_2 to $LiBH_4$ has been shown to lower the desorption temperature, aid reversibility but on the contrary reduce the storage capacity [43, 44].

2.7.2. Decomposition Pathways of Lithium Borohydride under Varying Pressure and Temperature

$LiBH_4$ has a melting temperature of 276 °C and decomposes into LiH, B and H_2 as shown in Equation 2 [45]; however different intermediate decomposition pathways have been proposed.

$$LiBH_4 \rightarrow LiH + B + \frac{3}{2}H_2 \qquad \text{Equation 2}$$

The first of these proposed decomposition pathways involves the intermediate $Li_2B_{12}H_{12}$, and is based on observations of the $B_{12}H_{12}$ bonds seen in both Raman [46] and Boron Nuclear Magnetic Resonance [47] measurements. The relevant decomposition pathway is shown in Equation 3. Temperatures in excess of 600 °C are required to decompose the stable intermediate $Li_2B_{12}H_{12}$.

$$LiBH_4 \rightarrow \frac{5}{6}LiH + \frac{1}{12}Li_2B_{12}H_{12} + \frac{13}{12}H_2 \rightarrow LiH + B + \frac{3}{2}H_2\,[45] \qquad \text{Equation 3}$$

The second pathway is via B_2H_6 and is based on measurements of diborane present in the decomposition of $LiBH_4$ as found by Kato et al. [48] and is show in Equation 4.

$$LiBH_4 \rightarrow LiH + \frac{1}{2}B_2H_6 \rightarrow LiH + B + \frac{3}{2}H_2 \text{ [45]} \qquad \text{Equation 4}$$

The final non-direct decomposition pathway encompasses both of the intermediates discussed above; firstly decomposing into diborane and then into $Li_2B_{12}H_{12}$ plus H_2. This pathway is shown in Equation 5.

$$2LiBH_4 + 5B_2H_6 \rightarrow Li_2B_{12}H_{12} + 13H_2 \text{ [45]} \qquad \text{Equation 5}$$

The production of both B_2H_6 and $Li_2B_{12}H_{12}$ directly reduces the reversibility of $LiBH_4$. The high thermal stability of $Li_2B_{12}H_{12}$ (stable up to 600 °C) coupled with B contained in B_2H_6 means that the levels of B and LiH available for recombination of $LiBH_4$ are lower and subsequently the amount of $LiBH_4$ reformed is lower than the initial amount. In order to optimise reversibility these intermediates must be avoided. It should also be noted that B_2H_6 is poisonous if inhaled.

By applying different pressure and temperature conditions it is possible to control the pathway by which $LiBH_4$ decomposes. For example by heating to a temperature of 600 °C and applying a H_2 over pressure of 50 bar, the direct decomposition into LiH and boron is suppressed enough such that decomposition via $Li_2B_{12}H_{12}$ is allowed; applying the same temperate under 0.1 bar H_2 means the intermediate $Li_2B_{12}H_{12}$ is unstable and full decomposition can take place [45].

2.7.3. Nano-confinement of $LiBH_4$

Nano-confinement of $LiBH_4$ within mesoporous carbon was shown by Cahen et al. [49] to eliminate the production of the $Li_2B_{12}H_{12}$ and B_2H_6 intermediates and not only reduce the onset temperature of hydrogen desorption in $LiBH_4$ from 300 °C to 200 °C but produce a singular desorption peak centred at 335 °C. Results also showed that although the desorption temperatures had been reduced the overall desorption enthalpy had not been affected by the confinement of the $LiBH_4$.

Cahen et al. [49] were able to produce the mesoporous carbon by infiltrating a SBA-15 (Santa Barbara Amorphous type material [50]) template with a sucrose solution ($C_{12}H_{22}O_{11}$) followed by heating to 900 °C to allow for the conversion of sucrose to carbon to take place. The silica template was removed using hydrofluoric acid leaving behind the mesoporous carbon. $LiBH_4$ was then impregnated into the carbon matrix using the Incipient Wetness Method [51].

Zhang et al. [52] also found by balling milling $LiBH_4$ nano-particles and disorder mesoporous carbon CMK-3 that $LiBH_4$ could be destabilized resulting in bulk hydrogen desorption at 332 °C. These results render nano-confinement of borohydrides an area of interest for hydrogen storage however further research is required to fully understand the underlying mechanisms involved.

2.7.4. Ball-milled Graphite with Lithium Borohydride Addition

In 2012, Zhang et al. [53] created a graphite+$LiBH_4$ composite via ball-milling. Milling was carried out under 3 bar H_2 for 10 h with a molar ratio of graphite-to-lithium borohydride of

2:1. Their results were quite impressive; compared to milled graphite alone, H_2 desorption increased by 3.7 wt% to 9.3 wt% along with a decrease in the hydrogen desorption onset temperature from 400 °C to 230 °C. Another achievement included no methane being desorbed. These results make a graphite+$LiBH_4$ composite an exciting material for hydrogen storage however the mechanisms behind these improvements in storage potential are unknown. Further work into this composite is required in order to develop an understanding of the underlying principle and to investigate the potential for reversible hydrogen storage.

3 Aims

Investigations will take place to determine and identify any catalytic effects of milled graphite on the hydrogen desorption mechanisms of $LiBH_4$. As a continuation from work carried out by Zhang et al. [53], investigations will be undertaken in attempt to discover a route for reversible hydrogen storage using a graphite+$LiBH_4$ system based on the success found in C-LiH systems for reversible hydrogen storage.

4 Experimental Procedure

4.1. Sample Preparation

4.1.1. Ball-milling Apparatus

Ball-milled graphite samples were prepared using a Retsch Planetary Ball Mill PM400. The mechanics involved in this process are described by Retsch; “The grinding jars are arranged eccentrically on the sun wheel of the planetary ball mill. The direction of movement of the sun wheel is opposite to that of the grinding jars in the ratio 1:-2 (or 1:-2.5 or 1:-3). The grinding balls in the grinding jars are subjected to superimposed rotational movements, the so-called Coriolis forces. The difference in speeds between the balls and grinding jars produces an interaction between frictional and impact forces, which releases high dynamic energies. The interplay between these forces produces the high and very effective degree of size reduction of the planetary ball mill.” [54]. Figure 4.1 shows the motion of the mill.

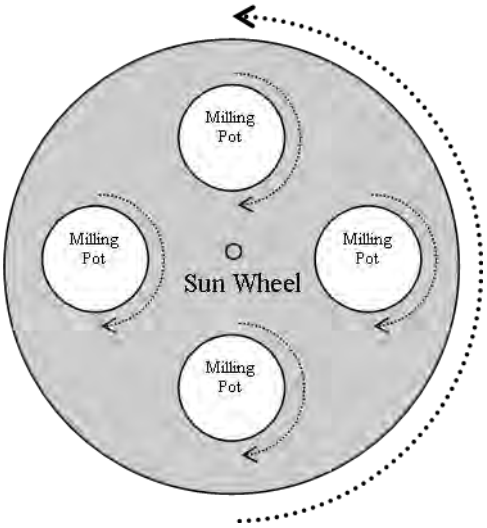

Figure 4.1. Motion of Retsch PM400 Planetary Ball Mill

A 250 ml tungsten carbide (WC) milling pot was used along with 10mm WC milling balls. In order to best recreate the conditions used by Zhang et al. [31], the same ratio of ball mass-to-sample mass of 13:1 was used. In order to reduce any contamination to the sample which could limit the ability to study the hydrogen adsorption and desorption properties of the graphite, the decision to use WC as a milling medium was chosen; the only contamination to be expected would be cobalt from the welding within the pot [22, 24, 31].

4.1.2. Ball-milled Samples

3.6 g of graphite powder (Sigma-Aldrich, -325 mesh, >99.99%) was weighed out and heated up to 150 °C at a heating rate of 2.5 °Cmin^{-1} and left to cool under vacuum in order remove any moisture or air present in the graphite. The graphite and milling balls were sealed inside the milling pot inside an Ar filled glove box. Finally the milling pot was evacuated and pressurised with 3 bar Hydrogen gas (Air products, 99.9995% purity H_2 gas), this process was repeated 3 times in order to reduce any remaining Ar prior to milling.

Ball-milling was performed at 280 rpm for a total of 8 h; the sample was milled for periods of 15 min of milling followed by 15 min of rest. This style of periodic milling was used to minimize the temperature increase of the graphite during milling due to the high impact/energy technique being used.

In order to maintain a constant milling pressure of 3 bar H_2, the pressure inside of the pot was checked and topped up. For every hour of milling the pot was transferred to a hydrogen charging rig and the H_2 pressure inside the pot topped up to 3 bar.

Once the pure graphite had been milled for 8 h, it was then split into 2 samples; 0.6 g of the hydrogenated 8 h milled graphite was taken for characterization, whilst the remaining 3 g was combined with $LiBH_4$ (Sigma-Aldrich, ≥95%) at a molar ratio of 2:1, graphite:$LiBH_4$.

The new sample was then milled independently for a further 2 h using the same milling process previously discussed; resulting in a total milling time of 10 h; the optimum milling time of graphite for maximum H_2 desorption with minimum hydrocarbon production as found by Zhang and Book [24].

All samples were handled and stored inside an Ar (BOC Gases, high purity Ar gas) filled glove box to avoid oxidation of samples.

4.2. Sample Characterisation

4.2.1. XRD

X-Ray Diffraction was used to study the crystallography/arrangements of atoms within a material. Each material has a unique diffraction pattern determined by the location of atoms within the lattice, i.e. separation and orientation, thus allowing for unknown materials within a sample to be identified. As the intensity of the peaks within the pattern is proportional to the degree of crystallinity of the material, it is also possible to trace how milling conditions affect graphite. Measurements were taken using a Bruker D8 Advance using Cu Kα (0.154nm) radiation looking between a 2θ range of 5-90 ° with a step size of 0.056 °. For the measurements taken at room temperature, samples were placed inside an air-tight silica Dome Cell under an Ar atmosphere in order to avoid oxidation. In-situ measurements were also taken using an Anton-Parr XRK900 cell; the samples were loaded into the cell in a He (Air

Products, ultra high purity He gas) atmosphere to avoid oxidation. Measurements were taken periodically up to 500 °C under 3 bar Ar at a heating rate of 5 °Cmin^{-1}.

Phase identification was conducted by comparison of obtained patterns to the ICDD PDF2 database (2011).

4.2.2. Raman Spectroscopy

Raman spectroscopy gives an insight in to the bonding types between atoms. Photons interact with molecules resulting in excitation from a ground or vibrational state to a "virtual state", as this energy level is not stable the molecule decays to a lower energy state emitting a photon. Differences between incident and scattered photon energies are equal to the difference between ground and vibrational states. Measurements were performed using a Renishaw InVia Reflex Raman Spectrometer; a 488nm excitation laser was focused though a x20 objective giving a spot size of 20 μm and a power of 2 mW. The samples were loaded directly into an Instec HCS621V cell inside an Ar filled glove box in order to prevent the sample's exposure to oxygen. Room temperature measurements were taken under an Ar atmosphere. In situ measurements were taken under a 100 mlmin^{-1} flowing Ar atmosphere in order to avoid the pressure inside the cell increasing as a result of H_2 desorption from the sample.

4.2.3. DSC

A Netzsch DSC 204 HP Phoenix was used to study the transitions taking place within samples during hydrogenation and dehydrogenation, in order to detect any reactions taking place. The DSC was situated inside an Ar filled glove box at atmospheric pressure and the samples placed in aluminium sample holders. Measurements were performed under both H_2

and Ar at a selection of pressures, all with a flow rate of 100 $mlmin^{-1}$. Samples were heated from room temperature up to the desired temperature where they were held isothermally for 20 min, before being cooled back down to room temperature; a heating/cooling rate of 2 $°Cmin^{-1}$ was used.

4.2.4. TPD

Temperature Programmed Desorption (TPD) was performed in conjunction with a Hiden Mass Spectrometer to analyse any gas desorbed during heating; and in particular to identify any H_2 or CH_4 release. The samples were inertly loaded into a quartz tube, and sealed inside the steel desorption vessel inside an Ar filled glove box. Ar was flowed over the sample at a rate of 100 $mlmin^{-1}$ and heated to 400 °C at a rate of 2 $°Cmin^{-1}$.

5 Results

5.1. Characterization of 8h Milled Graphite

5.1.1. Room Temperature XRD of As-Prepared 8h Milled graphite.

Room temperature (RT) XRD measurements were carried out under 1bar Ar using a domed silica cell, Figure 5.1. shows the XRD pattern, all the observed reflections are consistent with nanocrystalline graphite, the most dominant of which is the (002) peak located at 26.36 ° 2θ. This would suggest that no significant contamination has occurred during milling; however it is not possible to completely rule out any amorphous contaminants using XRD.

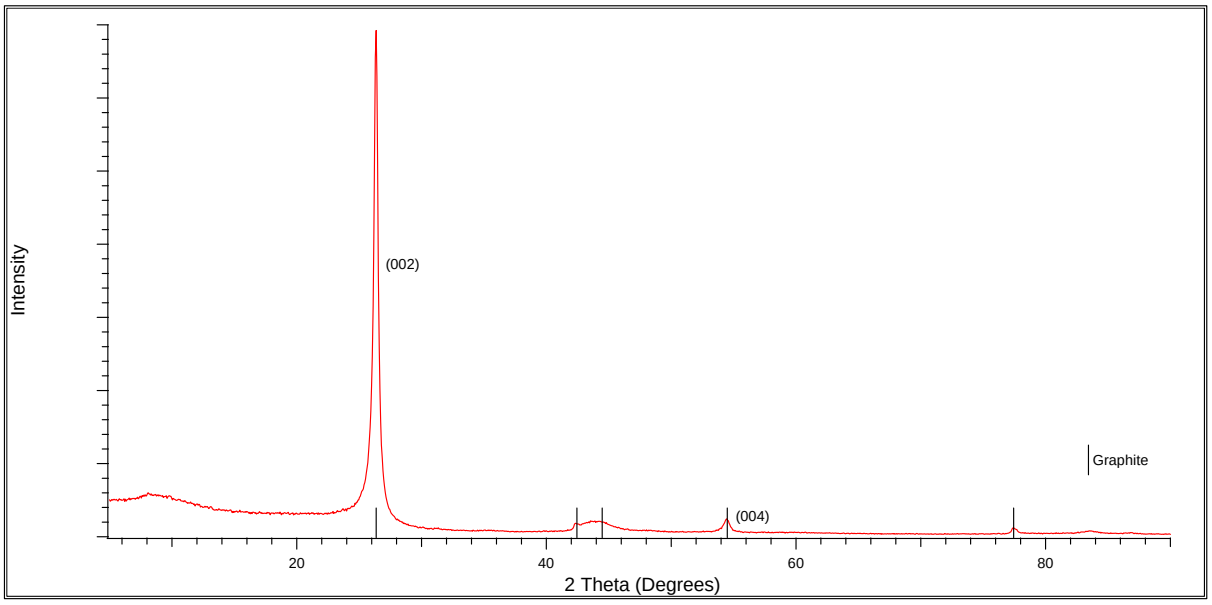

Figure 5.1. XRD pattern of 8 h milled graphite under 1bar Ar at room temperature; the thin black lines indicate the location of peaks associated with polycrystalline graphite

5.1.2. Room Temperature Raman Spectroscopy

Raman spectroscopy measurements were performed on the 8 h milled graphite sample under 1 bar Ar to investigate the bonding types present. Figure 2.2 shows the RT Raman spectra of 8 h milled graphite, the D and G peaks associated with sp^2 and sp^3 bonds are observed at 1353 cm^{-1} and 1577 cm^{-1} respectively. The D′ peak is present in the spectra and appears as a shoulder on the side of the G peak. The growth of the D and D′ peak due to milling, along with the G/D ratio indicate the production of mixture of nanocrystalline and amorphous graphite consistent with work by Zhang et al. [22, 24, 31, 53]. The G/D ratio for as-prepared 8 h milled graphite was calculated to be 1.14 indicating lattice deformation has occurred during milling.

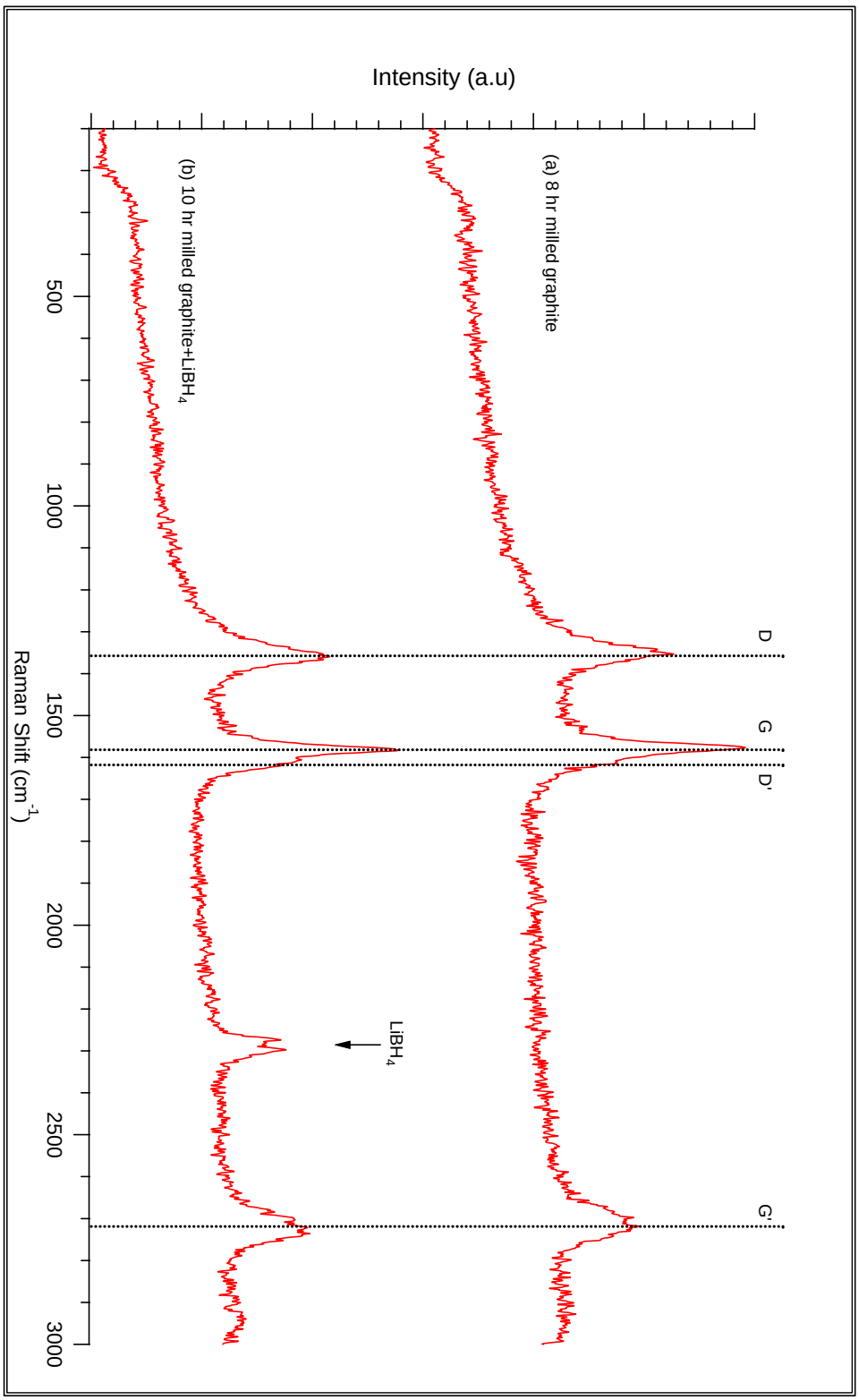

Figure 5.2. Room temperature Raman spectra of (a) 8 h milled graphite, (b) 10 h milled graphite+$LiBH_4$, under 1bar Ar

5.1.3. Decomposition of As-Prepared 8h Milled Graphite

A DSC trace of the decomposition of as-prepared 8 h milled graphite is shown in Figure 5.3.

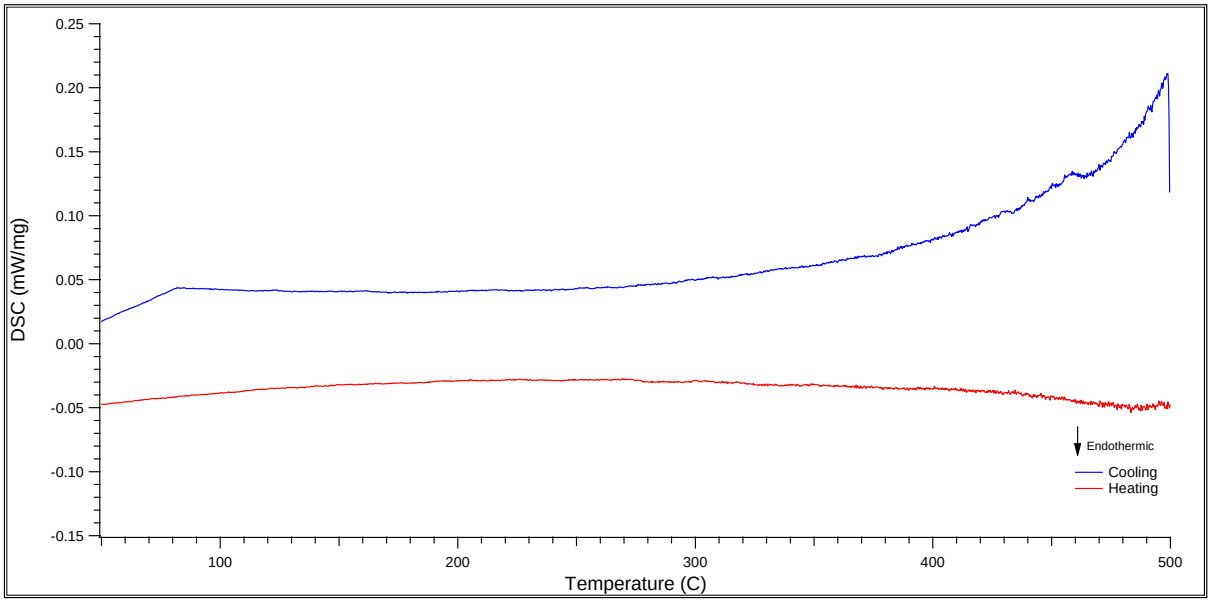

Figure 5.3. DSC decomposition of as-prepared 8 h milled graphite heated to 500 °C under 3 bar Ar

There were no obvious peaks observed in the DSC trace.

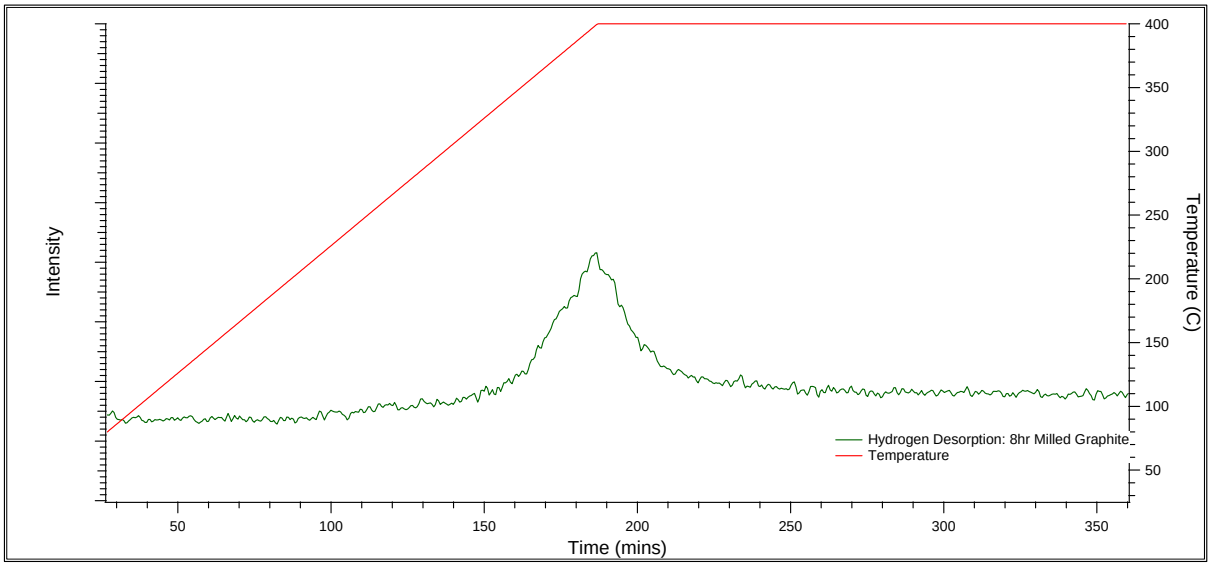

Figure 5.4. TPD results showing relative quantity of H_2 desorbed as a function of temperature and time for 8h milled graphite heated to 400 °C under 1 bar Ar

The green line in Figure 5.4 displays the amount of hydrogen desorbed by heating 8 h milled graphite to 400 °C (the intensity of the trace has been multiplied by a factor of 10 to allow for comparison to hydrogen desorption from graphite+$LiBH_4$). There is a small peak with an onset temperature of 350 °C which is centred at 400 °C. No methane was detected during heating which is consistent with work by Zhang et al. [31] who found that only graphite milled for 40 h under 3 bar H_2 desorbed methane upon heating.

5.2. Characterization of Graphite+$LiBH_4$

5.2.1. Room Temperature XRD of Graphite+$LiBH_4$

Room temperature XRD measurements were carried out under 1 bar Ar using a domed silica cell, Figure 5.5 shows the XRD pattern.

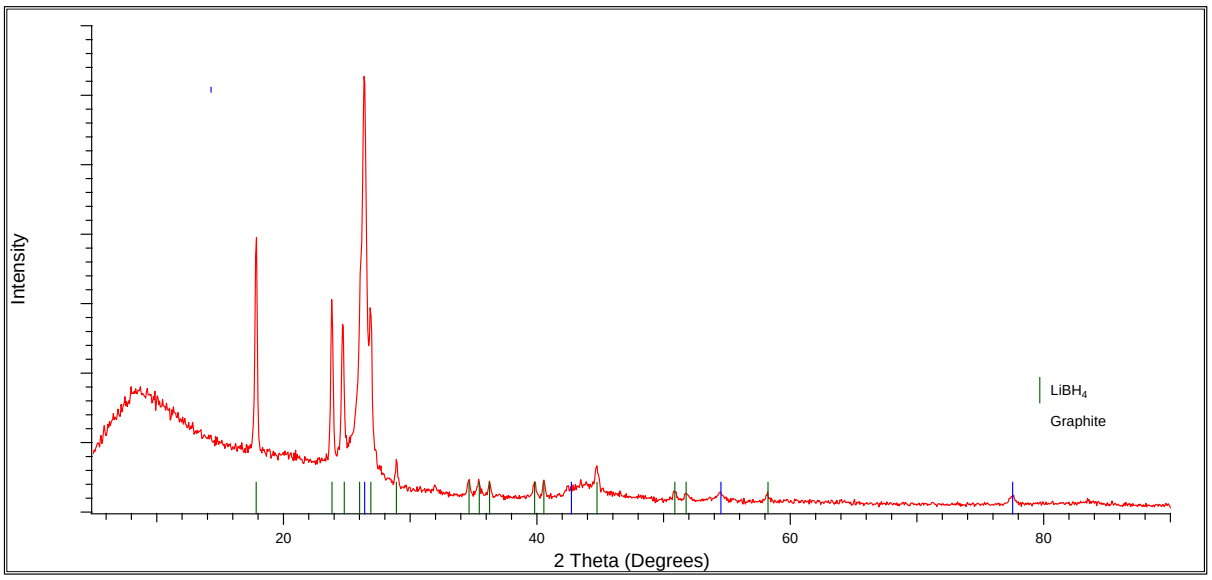

Figure 5.5. XRD pattern of milled graphite+$LiBH_4$ under 1 bar Ar at room temperature. The thin black lines indicate the location of XRD peaks associated with graphite, and the green lines indicate $LiBH_4$ XRD peak placement

Peaks associated with graphite and orthorhombic $LiBH_4$ are both present within the sample, while no peaks associated with contamination due to the WC milling medium were observed. The intensity of both the (002) and (004) peaks were reduced in comparison to the 8 h milled graphite. This reduction of intensity is due to further amorphisation of the graphite due to prolonged milling; the milling effect is well documented and discussed in Section 2.4.1.

5.2.2. Room Temperature Raman Spectroscopy of Graphite+$LiBH_4$

A room temperature Raman spectrum was collected for 10 h milled graphite+$LiBH_4$ under 1bar Ar to investigate the nature of the bonding. Figure 5.2 shows the resulting spectrum. As with the spectrum for 8 h milled graphite, the G, D, G′ and D′ peaks are present. The ratio of D/G of As-Prepared Graphite+$LiBH_4$ was calculated to be 0.86. This value is 0.28 lower than that of the D/G ratio of the 8 h milled graphite. This result directly indicates there is an increase in the amorphous graphite content within the sample induced from milling and the creation of sp^3 bonds. There is also a split peak centred around 2286 cm^{-1} which is associated with internal stretching of BH_4 bonds [42].

5.2.3. DSC Decomposition Profile of As-Prepared Graphite+$LiBH_4$

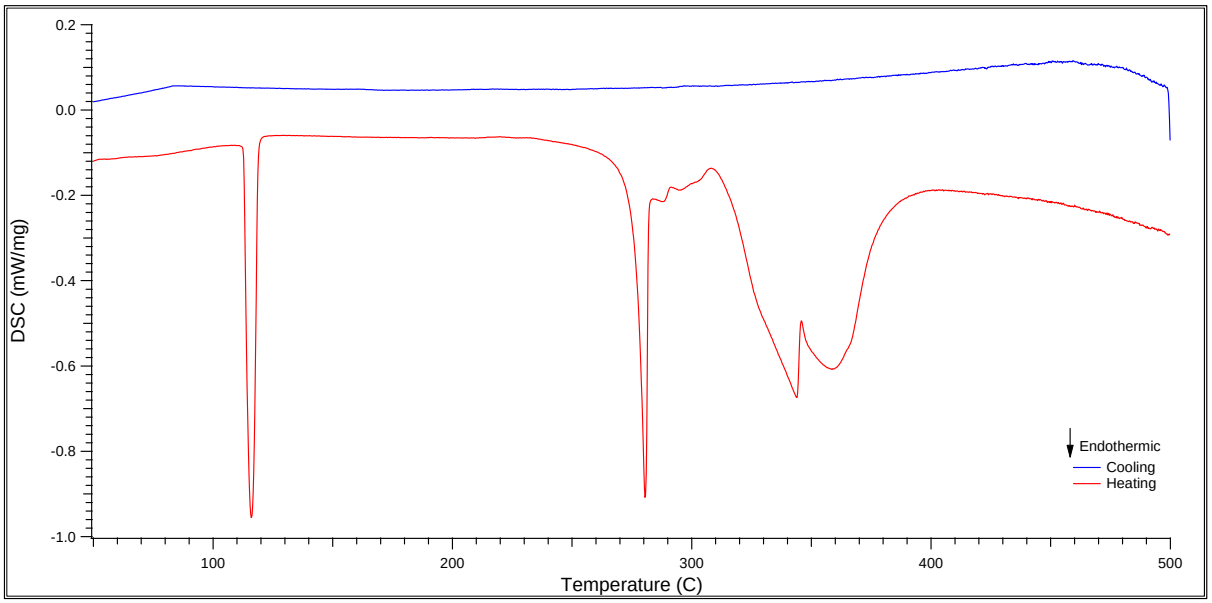

Figure 5.6. DSC of 10 h milled graphite+$LiBH_4$ heated at 2 °Cmin^{-1} to 500 °C, and then cooled, under 3 bar Ar flowing at 100 $mlmin^{-1}$

The DSC decomposition profile of graphite+$LiBH_4$ is shown in Figure 5.6. There are 4 major endothermic peaks visible on the trace. The first peak at 116 °C corresponds to the phase

change of $LiBH_4$ from orthorhombic to hexagonal, the second is attributed to melting at 280 °C, whilst the last two form a broad split-peak consistent with the decomposition of $LiBH_4$ and subsequent hydrogen desorption [41, 49, 55]. Both the phase change and melting temperatures are unaffected by the presence of graphite however the decomposition of $LiBH_4$ occurs at a lower temperature. Pure $LiBH_4$ starts to decompose at temperatures equal to that of its melting point, however significant desorption does not take place below 400 °C and is centred at 500 °C [41, 49, 55]. Figure 5.6 shows the decomposition peak to be centred at approximately 350 °C indicating that bulk desorption has been reduced by 150 °C and decomposition is completed by 400 °C. During this work it has not been possible to rule out any hydrogen evolution from the graphite itself but it can be confirmed from these results that milled graphite has a catalytic effect destabilizing $LiBH_4$.

There are two smaller endothermic peaks present on the trace between melting and bulk desorption at ~288 °C and ~295 °C respectively. The origin of these peaks is unknown, however the onset temperature of hydrogen desorption from $LiBH_4$ is 280 °C, and hence these peaks may be due to partial decomposition of the $LiBH_4$.

The blue line in Figure 5.6 shows the DSC trace during cooling after being heated up to 500 °C. If there was any $LiBH_4$ still present upon cooling, solidification and phase change peaks would be expected to be observed, hence it is suggested that all the $LiBH_4$ has decomposed during heating.

5.2.4. TPD of As-Prepared Graphite+$LiBH_4$

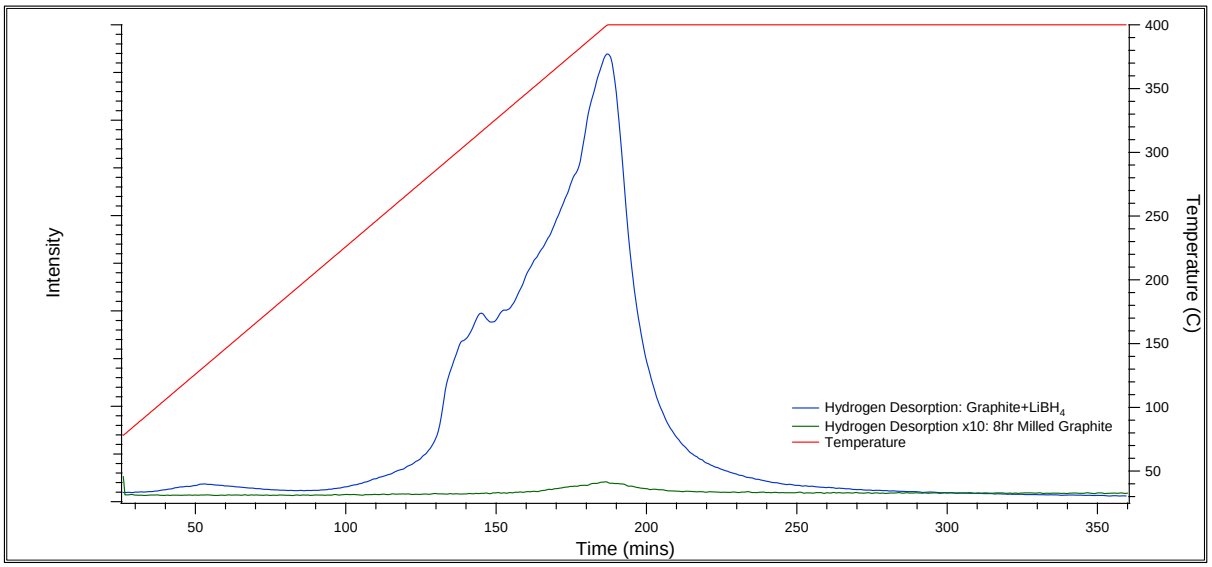

Figure 5.7. TPD of H_2 desorption as a function of temperature and time for 8 h milled graphite and graphite+$LiBH_4$ heated to 400 °C at 2 °Cmin^{-1} under 1 bar Ar

Figure 5.7 shows the TPD results for Graphite+$LiBH_4$ heated to 400 °C. There are three main peaks on the trace; the first peak at 131.7 °C, the second at 316.3 °C and the third at 400 °C. The desorption profile has the same features as seen in previous work [56]; an initial desorption due to the a phase transformation, a second desorption near the melting temperature and a third bulk desorption. However the profile in Figure 5.7 appears to be shifted up the temperature scale. This is believed to be due to a lag between the temperature of the furnace and the sample as previous analysis [49] has reported no such shifts in phase change and melting temperatures.

When the hydrogen desorption profile of Graphite+$LiBH_4$ is compared to 8 h milled graphite, it is clear that the amount of H_2 desorbed by the Graphite+$LiBH_4$ is significantly larger, and occurs at a lower temperature.

5.3. Investigation into the Decomposition of Graphite+$LiBH_4$ Sample

In order to further investigate the decomposition pathway of graphite+$LiBH_4$, DSC measurements were performed under 3 different pressures of H_2; 3 bar H_2 (Figure 5.8), 50 bar H_2 (Figure 5.9.) and 100 bar H_2 (Figure 5.10).

5.3.1. Decomposition of As-Prepared Graphite+$LiBH_4$ under 3 bar H_2

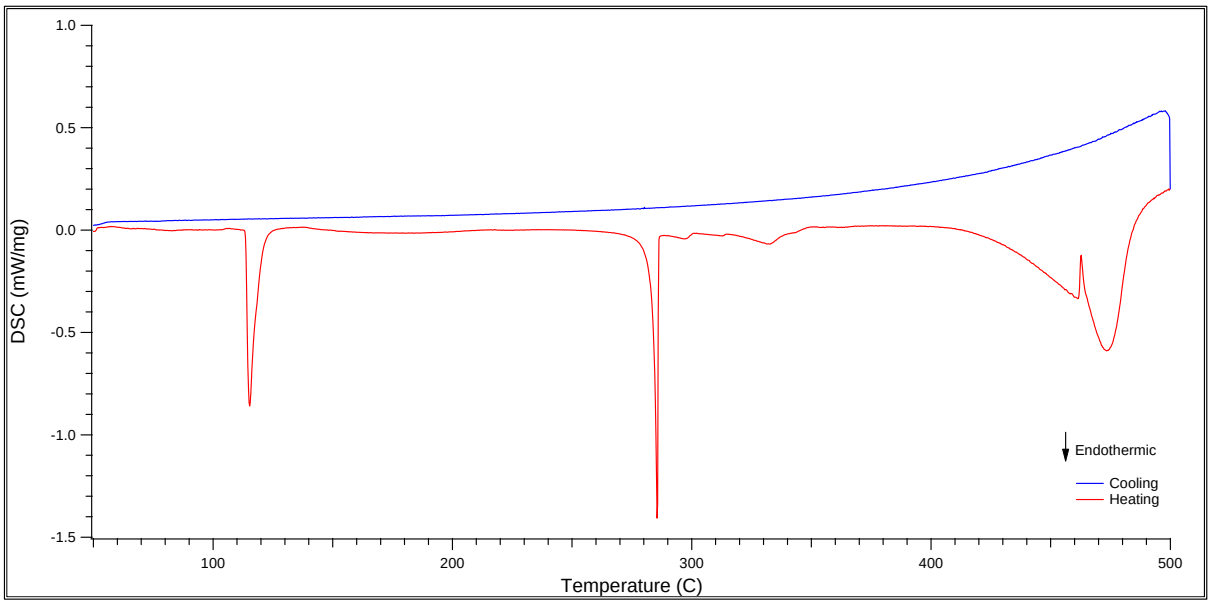

Figure 5.8. DSC of graphite+$LiBH_4$ heated to 500 °C at 2 °Cmin^{-1} under 3 bar H_2

Hydrogen above a pressure of 3 bar suppresses the decomposition of $LiBH_4$ (Figure 5.8) which now occurs at about 465 °C, over 100 °C higher than decomposition under 3 bar Ar. The melting temperature has also been increased from 280 °C to 285 °C. The section between fusion and the first half of the split decomposition peak on Figure 5.6 appears to be "stretched out" in Figure 5.8, suggesting that the kinetics of reactions have been slowed by the hydrogen over-pressure. Whereas the right hand half of the split peak in Figure 5.6 appears to be the

same as that under 3 bar H_2; indicating that the reaction kinetics are unchanged but that the reaction onset temperature is increased.

There are no peaks present in the cooling trace in Figure 5.8 indicating that although decomposition of $LiBH_4$ was suppressed by heating under 3 bar H_2, all of the $LiBH_4$ has decomposed.

5.3.2. Decomposition of Milled Graphite+$LiBH_4$ under 50 bar H_2

Figure 5.9. shows the DSC trace of graphite+$LiBH_4$ heated to 500 °C under 50 bar H_2. The most significant feature of the profile is that no decomposition peak is seen, suggesting that very little $LiBH_4$ has decomposed. This is confirmed when the cooling trace is inspected; both peaks associated with solidification and phase change are present confirming the presence of $LiBH_4$ after heating. An estimation of the amount of $LiBH_4$ remaining after heating can be made by calculating the ratio of the peak areas associated with the phase change during heating and cooling; under 50 bar H_2, 70% of the initial $LiBH_4$ is still present.

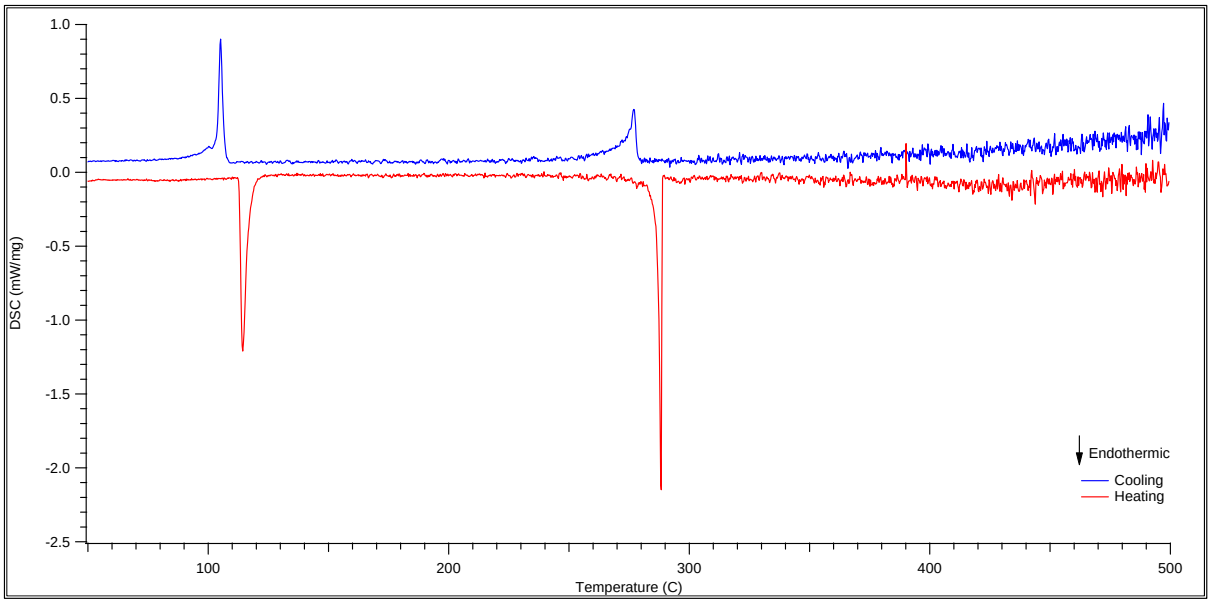

Figure 5.9. DSC decomposition profile of milled graphite+$LiBH_4$ heated to 500 °C at 2 °min^{-1} under 50 bar H_2

5.3.3. Decomposition of As-Prepared Graphite+$LiBH_4$ under 100 bar H_2

Figure 5.10 shows the DSC trace of heating Graphite+$LiBH_4$ under 100 bar H_2. This trace shows the same characteristics as heating to 500 °C under 50 bar H_2 with no decomposition peaks seen and the presence of $LiBH_4$ during cooling; using the same approximation as in Section 5.3.2, 83% of the initial $LiBH_4$ remains. This shows that by increasing the hydrogen over-pressure during heating, it is possible to suppress the decomposition of $LiBH_4$.

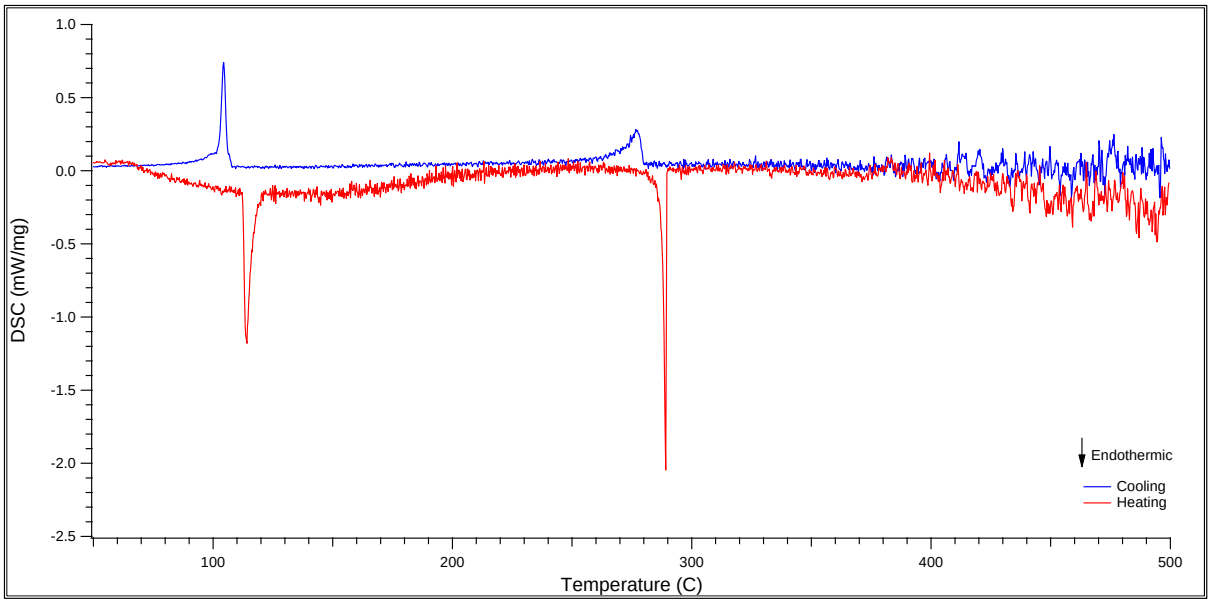

Figure 5.10. DSC of milled graphite+$LiBH_4$ heated to 500 °C at 2 °Cmin^{-1} under 100 bar H_2

5.3.4. Partial Decomposition of Milled Graphite+$LiBH_4$ under 3 bar Ar

The origin of the small endothermic peaks present between the melting of $LiBH_4$ and decomposition in Figure 5.6 is not clear. In order to try to understand the reactions taking place, samples were heated to 291 °C (after the first peak) or 308 °C (after the second peak) under 3 bar Ar at 2 °Cmin^{-1}, cooled to room temperature and then heated to 500 °C.

Figure 5.11 shows the DSC trace of graphite+$LiBH_4$ heated to 291 °C. No changes in the heating phase change peak or the melting peak were witnessed, however during cooling the phase change peak appears to be split. The origin of this split is unknown. In order to investigate this split peak, the same sample was re-heated to 500 °C under 3 bar Ar; the results are shown in Figure 5.12.

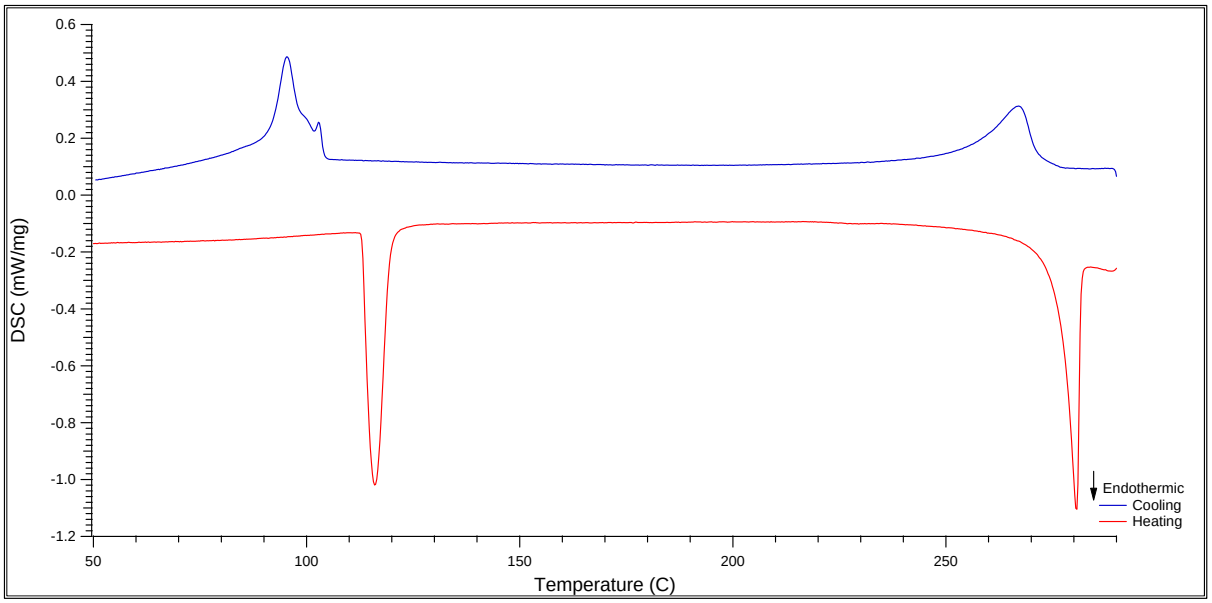

Figure 5.11. DSC trace of as-prepared graphite+$LiBH_4$ heated to 291 °C under 3 bar Ar

When the decomposition profiles in Figure 5.12. are compared, a few differences can be seen. Upon reheating, the split phase-change peak seen during initial heating to 291 °C is present. The peak associated with melting has widened and the peak location lowered by 4 °C to 276 °C. The double peak associated with decomposition of $LiBH_4$ has also been lowered by 10 °C compared to that of the as-prepared sample. When comparing the two graphs, the small endothermic peaks located between melting and decomposition have disappeared, suggesting that the reactions associated with the peaks had to take place before decomposition could occur.

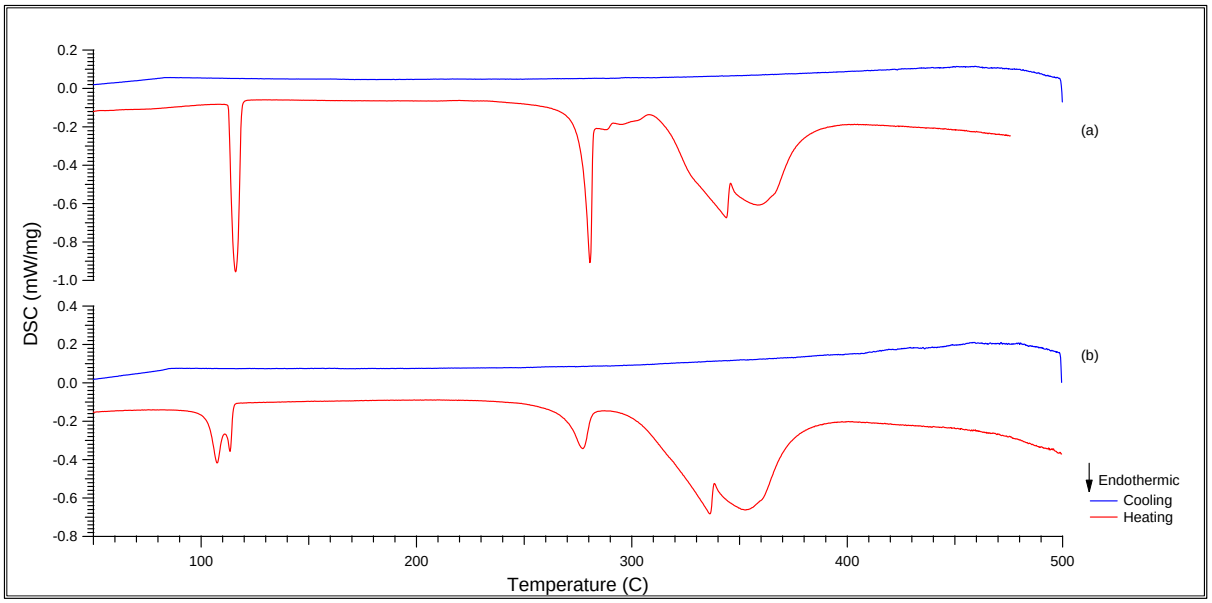

Figure 5.12. (a) DSC of milled graphite+$LiBH_4$ heated to 500 °C under 3 bar Ar (b) DSC of milled graphite+$LiBH_4$ that had previously been heated to 291 °C, heated to 500 °C under 3 bar Ar

Figure 5.13 shows the DSC trace of $LiBH_4$ heated to 308°C under 3bar Ar. This temperature is located just before decomposition after the small, unidentified endothermic peaks in Figure 5.6.

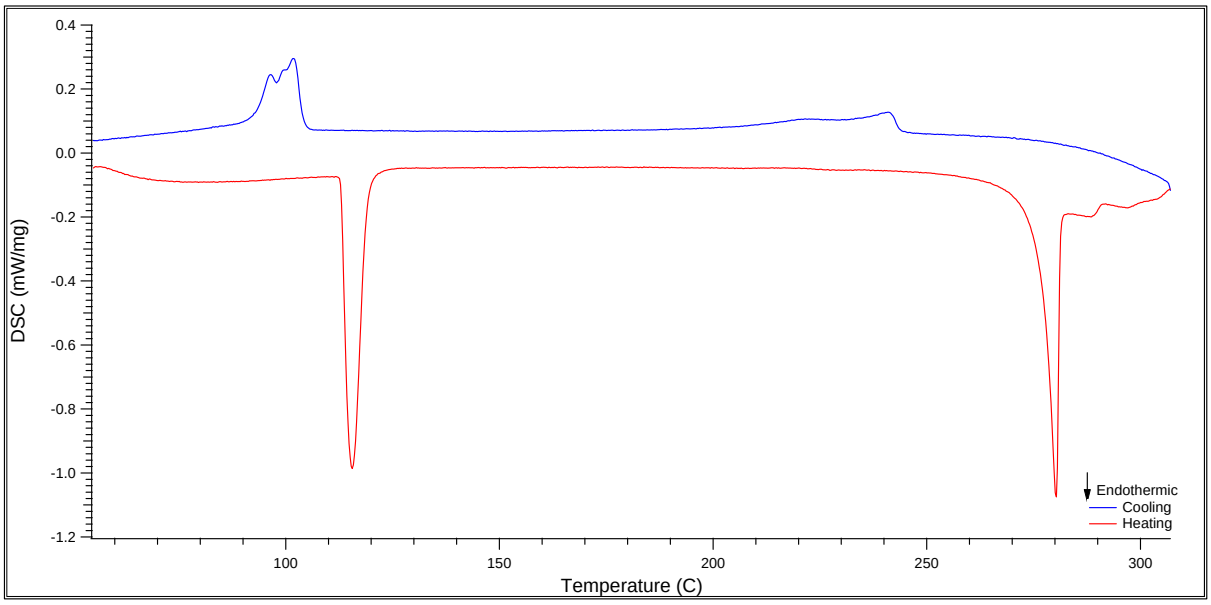

Figure 5.13. DSC heating trace of as-prepared graphite+$LiBH_4$ heated to 308 °C under 3 bar Ar

As expected, the phase change and fusion peaks observed during heating are consistent with full decomposition under the same conditions, and the small endothermic peaks are also present at the top of the temperature range at 288 °C and 297 °C. The peaks during cooling are no longer well-defined singular peaks as seen in Figure 5.10 where $LiBH_4$ decomposition is suppressed. This may be due to partial decomposition of $LiBH_4$ or nano-confinement within graphite.

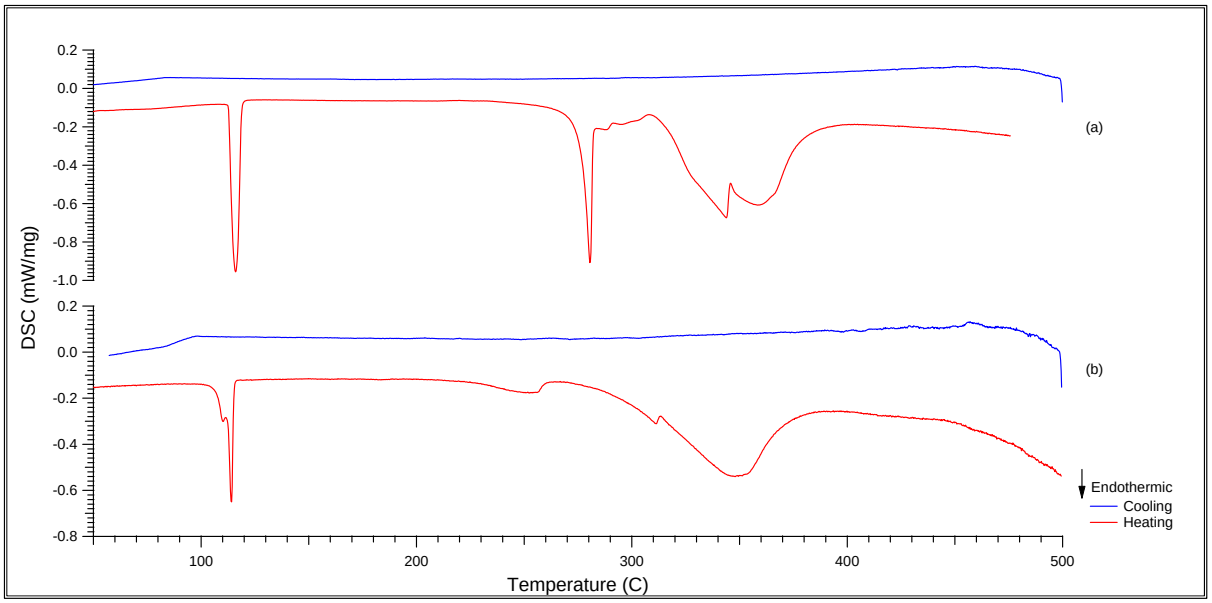

Figure 5.14. (a) DSC decomposition profile of as-prepared graphite+$LiBH_4$ heated to 500 °C under 3 bar Ar (b) DSC decomposition profile of graphite+$LiBH_4$ previously heated to 308 °C, heated to 500 °C under 3 bar Ar

Figure 5.14. shows the DSC trace of graphite+$LiBH_4$ that has been heated up to 308 °C before being cooled and reheated to 500 °C. The split phase change peak witnessed during cooling after heating to 308 °C is observed at 114 °C, however the melting peak of $LiBH_4$ has decreased from 280 °C to 253 °C. The decomposition peak is centred on 348 °C which is only 2 °C lower than decomposition of the as-prepared sample.

When Zhang et al. [52] were able to support $LiBH_4$ nano-particles in disordered mesoporous carbon (nano-$LiBH_4/C_{mesosporous}$) they recorded similar results as to that shown in Figure 5.14. The melting temperature of $LiBH_4$ was lowered to 270 °C and bulk desorption was between 293 °C and 400 °C. These similar results suggest that during heating of as-prepared graphite+$LiBH_4$ between the temperature range of 280 °C and 310 °C $LiBH_4$ may intercalate between the graphene layers forming nano-dispersed $LiBH_4$ similar to that of Zhang et al. Another possibility is that the $LiBH_4$ becomes trapped in pores within graphite.

5.3.5. Investigation into the Splitting of the Phase Change Peak in As-prepared Graphite+$LiBH_4$ During Heating

To try to understand the development of the split phase-change peak, samples were heated to 291 °C and 308 °C before being heated to 500 °C under 100 bar H_2. Figure 5.15. shows the results for graphite+$LiBH_4$ previously heated to 291 °C and Figure 5.16. shows the results for graphite+$LiBH_4$ previously heated to 308 °C.

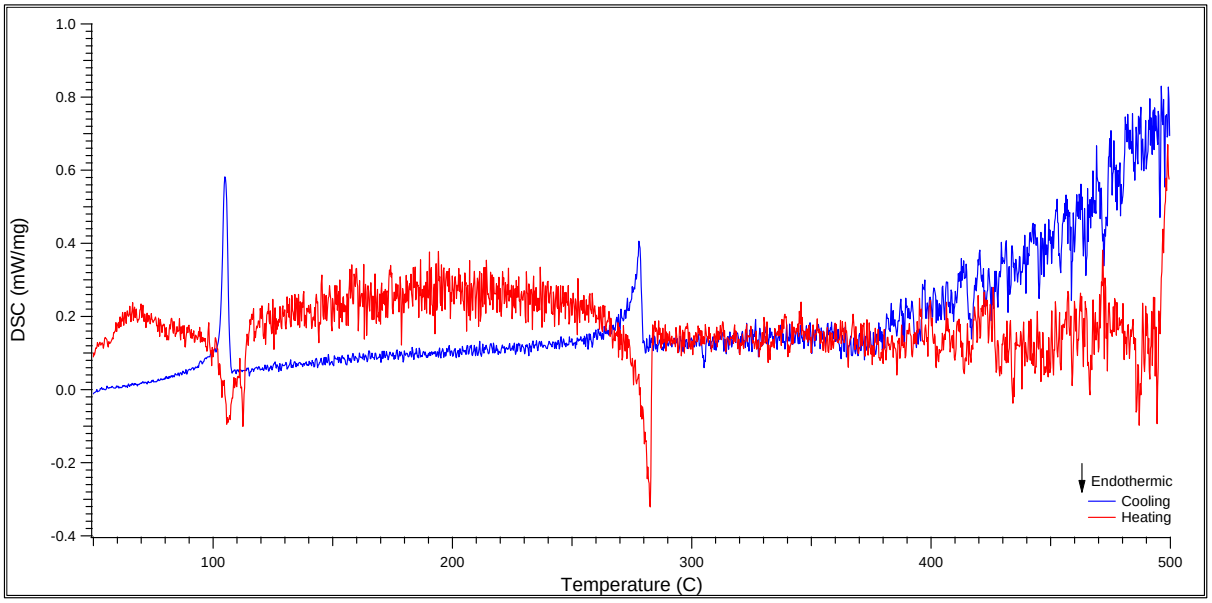

Figure 5.15. DSC trace of graphite+$LiBH_4$ previously heated to 291 °C under Ar, heated to 500 °C under 100 bar H_2

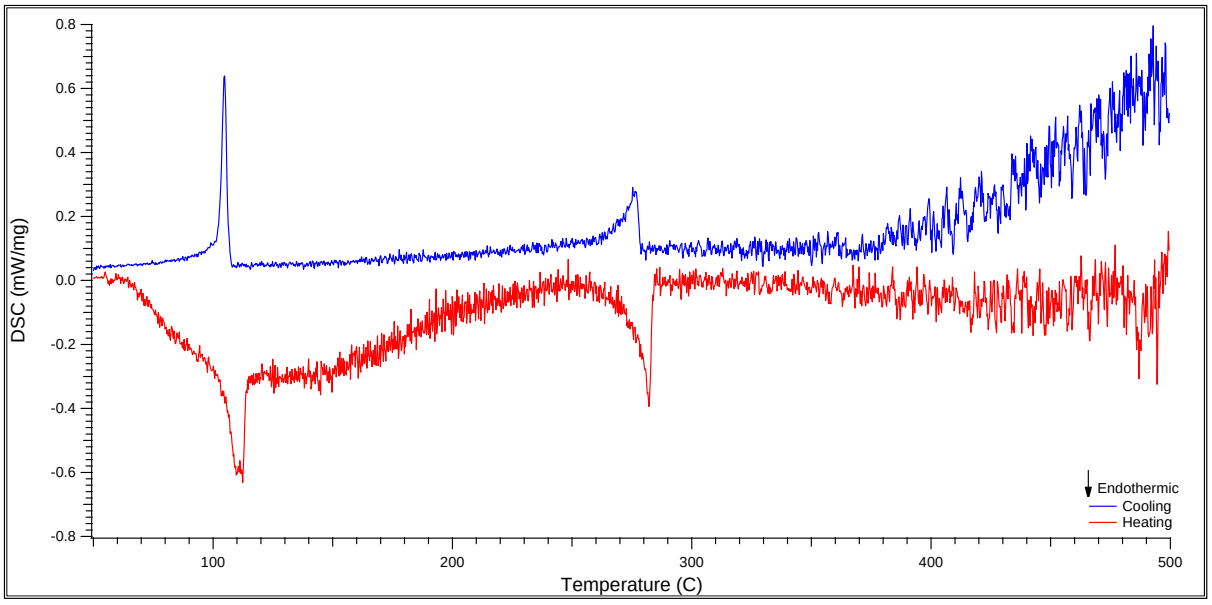

Figure 5.16. DSC trace of graphite+$LiBH_4$ previously heated to 308 °C under Ar, reacted to 500 °C under 100 bar H_2

Both traces show the same characteristics in their heating and cooling profiles. The split phase change peak is visible during heating and both melting peaks are centred at 282 °C. The most significant feature of these plots is the singular sharp phase-change peak present at 105 °C during cooling. This implies that the partially decomposed sample ($LiBH_{4-\varepsilon}$) may have recombined with H_2 under pressure to reform $LiBH_4$.

5.3.6. Investigation into Decomposition of As-Prepared Graphite+$LiBH_4$ using In-situ Raman Spectroscopy

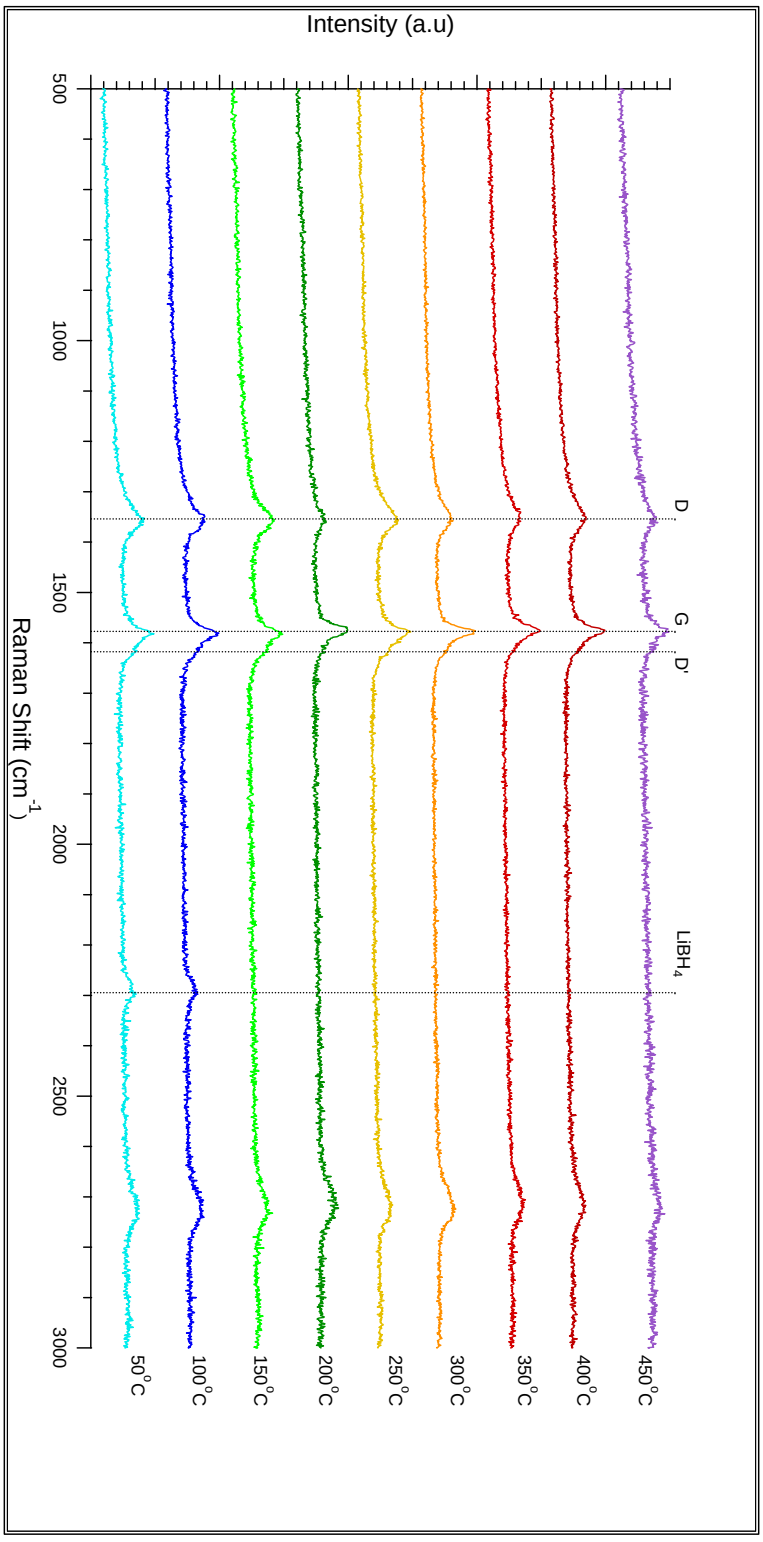

Figure 5.17. In-situ Raman spectroscopy of as-prepared graphite+$LiBH_4$ heated at 2 °Cmin^{-1} under 1 bar flowing Ar

Figure 5.17. shows in-situ Raman spectroscopy measurements of as-prepared graphite+$LiBH_4$ heated to 450 °C in steps of 50 °C at a heating rate of 2 °Cmin^{-1}. The D, G, D′ and G′ peaks of carbon are present throughout the scanning suggesting that the graphite acts as a catalyst destabilizing $LiBH_4$. The peak located at 2295 cm^{-1} is due to the stretching of BH_4 bonds of $LiBH_4$ and appears in the first two scans (50 °C and 100 °C) after which the peak is no longer detected. This is a result of the phase change of $LiBH_4$ from the orthorhombic to the hexagonal phase at 116 °C.

5.3.7. In-situ XRD Measurements of the Decomposition of As-Prepared Graphite+$LiBH_4$

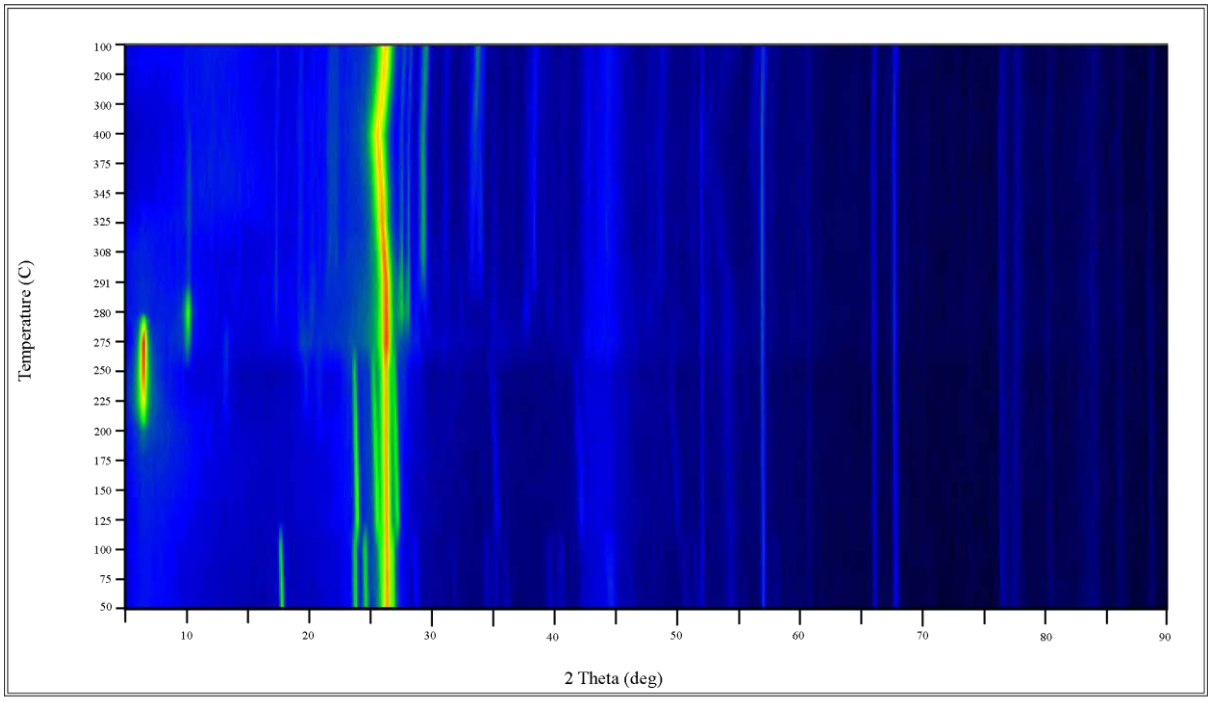

Figure 5.18. XRD contour plot showing in-situ measurements of graphite+$LiBH_4$ heated to 400 °C degrees at a heating rate of 2 °Cmin^{-1}. Colour is proportional to count intensity; black implying a minimum and red a maximum

Figure 5.18 shows in-situ XRD of graphite+$LiBH_4$ heated to 400 °C. The consistent peaks present throughout heating and cooling are produced by reflections from graphite and Al_2O_3 (sample holder). During heating, the intense peak at 26.36 ° 2θ corresponding to the (002) peak of graphite, does not shift location until temperatures exceed 270 °C; this is unexpected as during heating the graphite lattice expands resulting in a shift in peak position to a lower 2θ value.

At 200 °C a phase change takes place relating to reflections seen at 6.23 ° 2θ before undergoing another phase transition at 280°C. Another phase located at 10.16 ° 2θ is present between 250 °C and 291 °C. Figure 5.19. shows the XRD of graphite+$LiBH_4$ at 275 °C in which both unknown phases are simultaneously present; 6.62 ° 2θ and 10.16 ° 2θ.

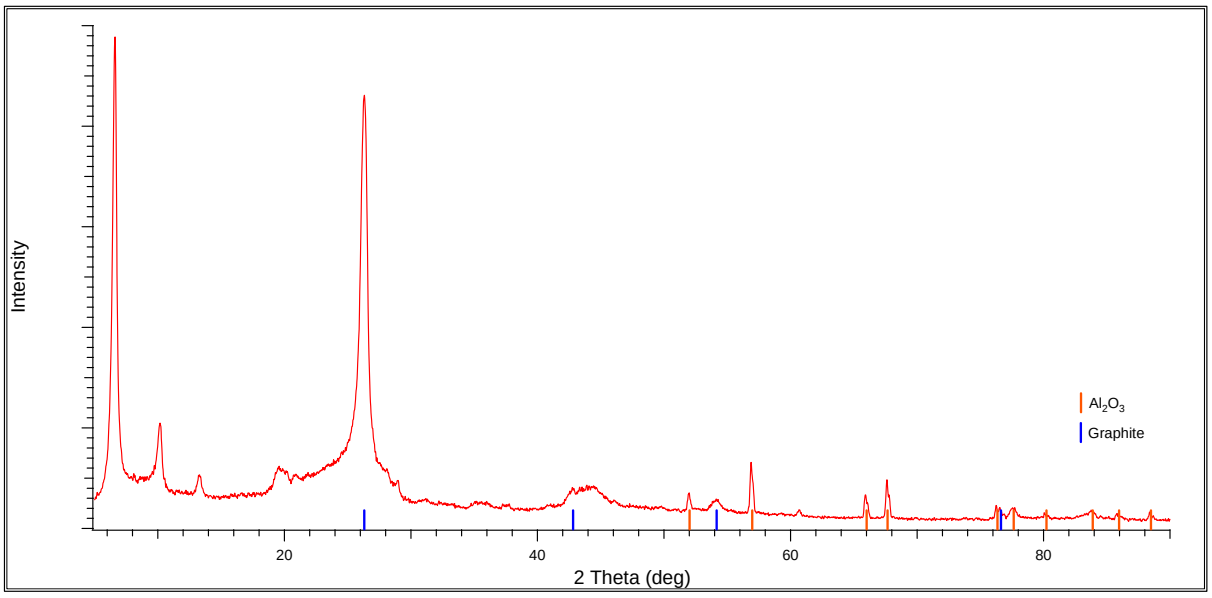

Figure 5.19. XRD measurement of graphite+$LiBH_4$ heated to 275 °C, displaying peak locations of Al_2O_3 (sample holder) and graphite

Once the sample had been heated to 400 °C, it was cooled to room temperature. Figure 5.20 shows the resulting XRD pattern after cooling.

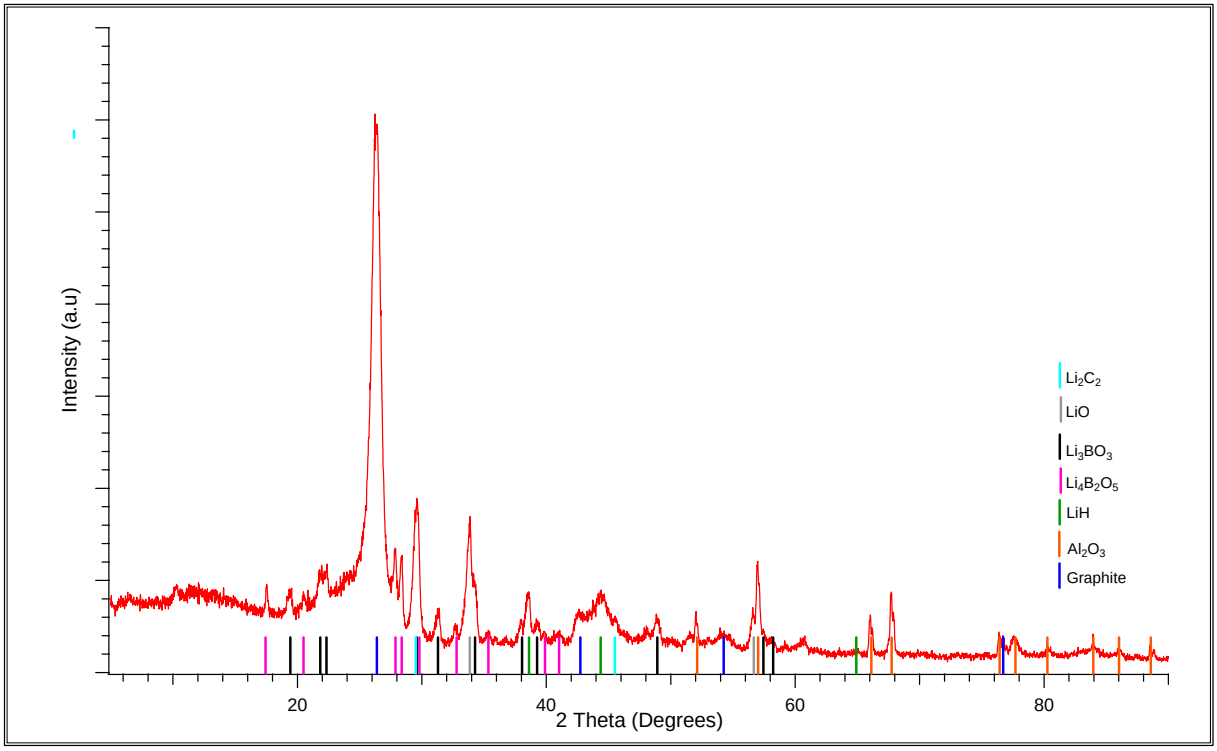

Figure 5.20. XRD measurement of graphite+$LiBH_4$ heated to 400 °C and cooled to room temperature

Upon characterization of the sample it was found to contain lithium oxide, and two types of lithium borate. Subsequently it is apparent that the sample was exposed to air at some stage, the origin of this is unknown. It should also be noted that traces of lithium carbide are present. When Ichikawa et al. [39] reversibly stored H_2 in a graphite and lithium hydride nanocomposite, the reversibility of the reaction relied upon the formation of Li_2C_2 during dehydrogenation. The finding of this in the dehydrogenated sample suggests that reversible storage of H_2 in a graphite+$LiBH_4$ composite may be possible.

The intermediate $Li_2B_{12}H_{12}$ was not detected suggesting that the presence of graphite suppresses its formation.

Using the in-situ XRD data, lattice expansion in the c plane of graphite was plotted as a function of temperature; results are shown in Figure 5.21.

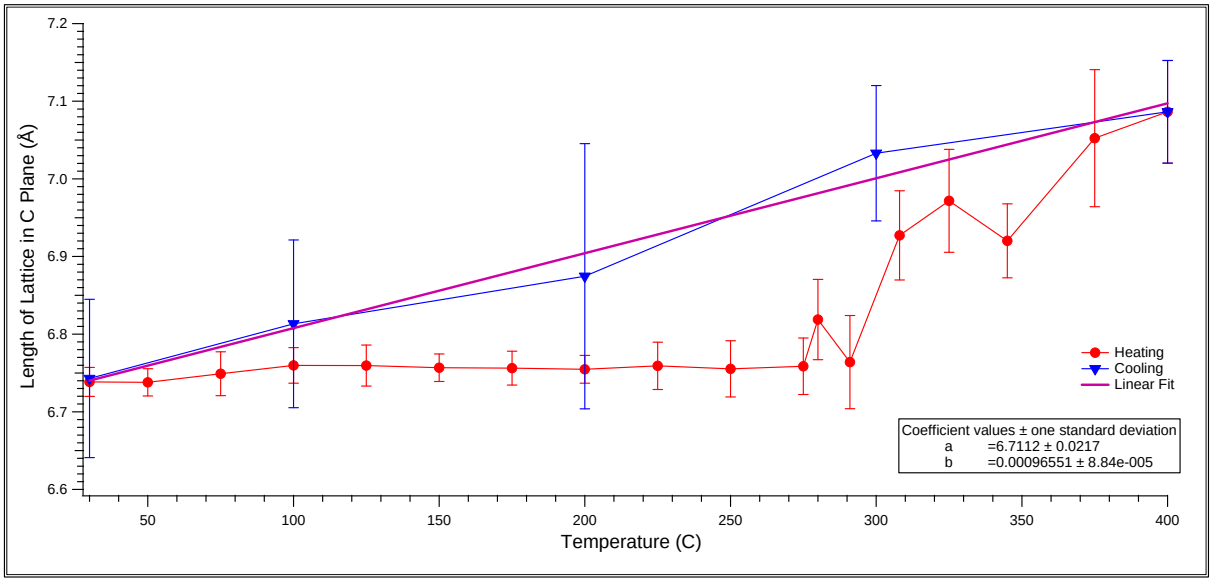

Figure 5.21. Lattice parameter (C) of graphite as a function of temperature (from Figure 5.18)

During heating no expansion occurred until 275 °C when rapid expansion takes place. During cooling contraction is almost linear as is expected for both expansion and contraction. Expansion of the graphite lattice in the c plane is directly proportional to temperature [57], however, in the graphite+$LiBH_4$ sample expansion appears to be suppressed during heating to 275 °C. This could be due to nano-confinement of $LiBH_4$ during ball-milling, in which the $LiBH_4$ holds the lattice tight opposing expansion. At temperatures similar to the melting point (280 °C) of $LiBH_4$ lattice expansion begins. As desorption occurs at temperatures in the region of 300 °C, the lattice rapidly expands; this may be due to the decomposition of $LiBH_4$ within the graphite lattice, allowing expansion to finally take place.

5.4. Investigation of Reversible Hydrogen Storage in Milled Graphite+$LiBH_4$

5.4.1. DSC Measurements

Figure 5.22 shows the DSC traces of as-prepared graphite heated to 400 °C under 3 bar Ar and cooled to room temperature before being rehydrogenated by heating to 500 °C under 100 bar H_2 and held isothermally for 20 min and cooled, finally the sample was dehydrogenated by heating to 500 °C under 3 bar Ar. The 1st dehydrogenation is consistent with initial decomposition measurements as shown in Figure 5.6. During rehydrogenation no peaks are seen during heating, however, two exothermic peaks are present during cooling; 104.5 °C and 252 °C. The peak at 104.5 °C is believed to be a result of the hexagonal to orthorhombic phase transformation of $LiBH_4$, whilst the peak at 252 °C is believed to be due to solidification of $LiBH_4$. Upon reheating under 3 bar Ar, 3 exothermic peaks are visible; 114 °C, 254 °C and 462 °C. The first peak is suspected to be a phase change, the second melting and third decomposition and thus hydrogen evolution. These results suggest that 10 h milled graphite+$LiBH_4$ is able to reversibly store hydrogen over at least one cycle. An estimation of the amount of $LiBH_4$ reformed during rehydrogenation can be calculated using the ratio of phase change peak areas from the 1st and 2nd dehydrogenation traces: this leads to an estimated reformation of 18.5% of the initial amount of $LiBH_4$.

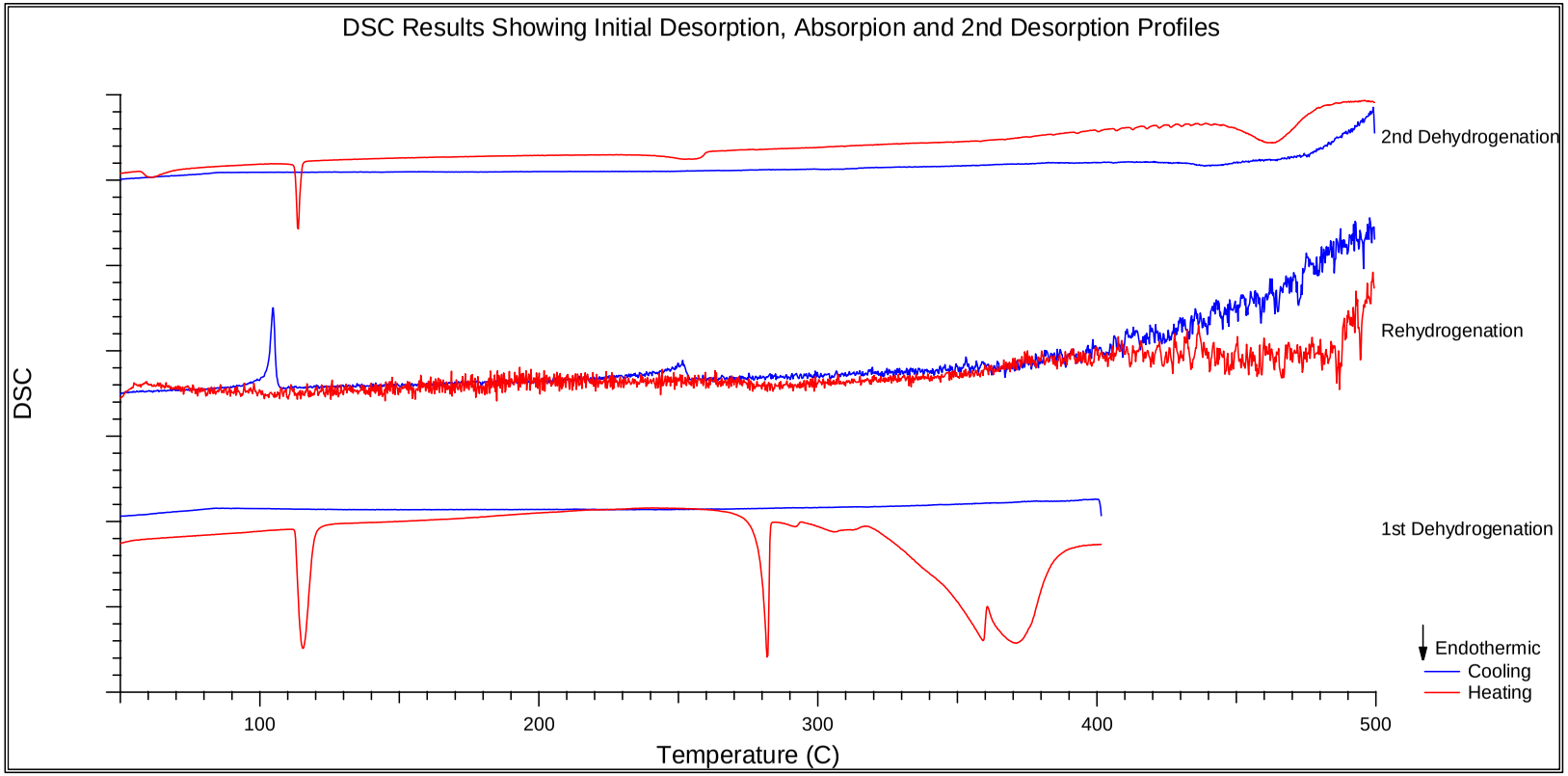

Figure 5.22. DSC traces of as-prepared graphite+$LiBH_4$ heated to 500 °C under 3 bar Ar, heated to 500 °C under 100 bar H_2 and then reheated to 500 °C under 3 bar Ar for investigation into reversible hydrogen storage

6 General Discussion

XRD analysis of both samples (Figure 5.1. and Figure 5.5) showed diffraction patterns with no contamination such as Co or WC from the milling medium. The (002) and (004) graphite peaks were present in both samples, indicating the milled graphite still retained some degree of crystallinity. However the intensity of both peaks greatly decreased as a result of further milling in the graphite+$LiBH_4$ sample indicating that additional milling had increased the amorphous:crystalline graphite ratio.

It has been shown using Raman spectroscopy (Figure 5.2) that the ball-milling of graphite leads to the breaking down of graphene layers and creation of a crystalline/amorphous mixture. Milling time has a direct effect on the level of amorphisation and the number of sp^3 bonds created; this was apparent from the decrease in the D/G peak ratio by 0.28 (from 1.14 to 0.86) as a result of an additional 2 h of milling under 3 bar H_2. The graphite+$LiBH_4$ trace displayed a peak centred at 2286 cm^{-1}; this was identified as the internal stretching of BH_4 bonds in $LiBH_4$.

Differential Scanning Calorimetry was carried out on both samples; samples were heated to 500 °C under 3 bar Ar. The 8 h milled graphite trace did not show any peaks suggesting no reactions with quick kinetics taking place during heating or cooling. This result agreed with work by Zhang et al. [31] for graphite milled for 40 h under 3 bar H_2; they noted that due to high thermal stability of C-H bonds that no hydrogen desorption occurred below 400 °C and substantial desorption did not occur until after 500 °C. Temperature Programmed Desorption (TPD) results for 8 h milled graphite (Figure 5.4) showed no hydrogen release until above

350 °C where a small amount was desorbed centred at 400 °C. No methane desorption was detected.

DSC on the 10h Milled Graphite+$LiBH_4$ (Figure 5.6) identified 4 large endothermic peaks during heating. The first at 116 °C corresponds to the orthorhombic to hexagonal phase change of $LiBH_4$, the second at 280° C is attributed to the melting of $LiBH_4$ and the last two form a split peak which is associated with the decomposition of $LiBH_4$ and H_2 desorption [41, 49, 55]. This split peak indicates a two-step reaction with each step having equally quick kinetics. Both the phase change and melting peaks were unaffected by the presence of graphite, however the decomposition temperature was decreased by 150 °C to 350 °C, implying that graphite has a catalytic effect upon $LiBH_4$ destabilizing its thermal stability. No peaks were present during cooling suggesting that all $LiBH_4$ had decomposed. Two small endothermic peaks were present on the heating trace between melting and decomposition, the origin of which are unknown. The hydrogen desorption onset temperature of $LiBH_4$ is 280°C, so it is possible these peaks were a result of partial decomposition of $LiBH_4$. TPD results showed 3 hydrogen desorption peaks and no methane emission. The 3 peaks were located at 132 °C, 316 °C and 400 °C; these peaks are believed to be a result of the phase change, melting and decomposition of $LiBH_4$ respectively[56]. The desorption profile appeared to be shifted to higher temperature; this was believed to be due to a lag between the increase in temperature of the furnace and the sample. DSC measurements indicated that desorption temperatures were lower.

Further investigation into the dehydrogenation of graphite+$LiBH_4$ was carried out, samples were heated to 500 °C under 3 bar H_2 (Figure 5.8), 50 bar H_2 (Figure 5.9.) and 100 bar H_2

(Figure 5.10). It was found that when heating under a hydrogen pressure greater than 3 bar, the melting temperature increased and decomposition was suppressed. Applying a pressure of 3 bar H_2 resulted in desorption being delayed by over 100 °C, whereas pressures of 50 bar and 100 bar resulted in suppression of $LiBH_4$ decomposition. This may provide an effective way to study the phase change and fusion of $LiBH_4$ at high temperature, avoiding any decomposition.

To further investigate the decomposition of graphite+$LiBH_4$, samples were heated to 291 °C and 308 °C under 3 bar Ar, and then reheated to 500 °C under the same pressure conditions. Upon cooling after partial heating, a split in the phase change peak was detected. During reheating for both samples, split phase-change peaks were identified, along with a decrease in the melting temperature and onset temperature of decomposition. The split phase-change caused by partial heating may be a result of partial decomposition of $LiBH_4$, the decomposition profile of the reheated samples suggested the possibility of nano-confinement of $LiBH_4$ within graphite. Zhang et al. [52] were able to confine nano-$LiBH_4$ in mesoporous Carbon, their DSC results showed similar qualities with the melting peak being shifted to lower temperatures and less pronounced, with decomposition centred at 350 °C. The small endothermic peaks seen in the dehydrogenation DSC profile of graphite+$LiBH_4$ under 3 bar Ar may be a combination of partial decomposition of $LiBH_4$ and a subsequent intercalation of the $LiBH_4$ into the graphene layers.

To further investigate the possibility of partial decomposition, samples were heated to 291 °C and 308 °C in 3 bar Ar, before being heating to 500 °C under 100 bar H_2 (Figure 5.15. and

Figure 5.16.). Results showed that after heating under hydrogen, the phase change peak returned to a sharp singular peak suggesting that the partial decomposition of $LiBH_4$ was their origin.

In-situ X-Ray Diffraction measurements were taken for graphite+$LiBH_4$ heated to 500 °C under flowing 100 $mlmin^{-1}$ He (Figure 5.18). During heating the (002) graphite peak did not appear to shift until temperatures exceeded 270 °C. Thermal lattice expansion in the c plane is normally linear suggesting that the expansion was suppressed. Two phases (6.62 ° 2θ and 10.16 ° 2θ) were detected at 200 °C and 250 °C whose origins were unknown; these phases then disappeared upon further heating to 280 °C and 290 °C respectively.

Characterization of the dehydrogenated sample indicated that oxidation had occurred; LiO, Li_3BO_3 and $Li_4B_2O_5$ were all present in the XRD pattern. Oxidation was believed to have occurred during decomposition whilst inside the Anton Paar cell. It is believed that the underlying decomposition mechanism was affected by the presence of oxygen as it reacted with Li. Diffraction peaks associated with the sample holder (Al_2O_3) were detected.

Reflection due to Li_2C_2 were also detected in the XRD patterns of the desorbed sample suggesting the option for a reversible hydrogen storage system based on work by Ichikawa et al. [39] which used the formation of Li_2C_2 as an important part of the reversible reaction.

Analysis of the XRD patterns allowed the expansion in the c plane of graphite to be investigated (Figure 5.21). Results showed insignificant expansion for temperatures below 275 °C and a rapid expansion thereafter. The suppression of lattice expansion maybe a result of intercalated $LiBH_4$ within the lattice as a result of milling, after temperatures equal to that of the melting point of $LiBH_4$ expansion occurs; this may be a result of decomposition of $LiBH_4$ thus allowing the lattice to finally expand, however this is just speculation.

In-situ Raman spectroscopy results of graphite+$LiBH_4$ were carried out. The D, G, D′ and G′ peaks are present though out heating suggesting that the graphite does not react with the $LiBH_4$ and merely acts as a catalyst. The peak associated with the stretching of BH_4 bonds disappeared for temperatures above 100 °C; this was believed to be due to the orthorhombic to hexagonal phase change which occurs at 116 °C.

Finally, DSC was used to investigate reversibility in the graphite+$LiBH_4$ sample. The sample was dehydrogenated at 400 °C under 3 bar Ar, then heated to 500 °C under 100 bar H_2 for rehydrogenation before a second dehydrogenation was performed under 3 bar A. During cooling in the rehydrogenation step, peaks consistent with solidification and phase change of $LiBH_4$ were present implying that recombination had occurred. In the 2^{nd} dehydrogenation peaks consistent with phase change and melting of $LiBH_4$ were present with a decomposition peak occurring at 462 °C. Although decomposition occurred at a much higher temperature (111 °C higher) than for the as-prepared sample this results suggest that graphite+$LiBH_4$ may provide a reversible hydrogen system. An estimation of the amount of $LiBH_4$ that had recombined was calculated by taking a ratio of the phase change peak areas of 1^{st} and 2^{nd} dehydrogenation, the system was estimated to recombine 18.5% of the initial $LiBH_4$ in the sample.

The presence of Li_2C_2 in the dehydrogenated sample suggests that a similar reversible system to that described by Ichikawa et al. [39] for graphite+LiH is taking place. The $LiBH_4$ first breaks down in to LiH, B and H_2 before the LiH reacts with the graphite to form Li_2C_2 and H_2. Subsequently the rehydrogenation conditions used by Ichikawa et al. should be the basis of investigations to form a reversible (hydrogen cycling) system.

The graphite+$LiBH_4$ composite has shown potential as a new material for H_2 storage. The ball-milling of $LiBH_4$ with hydrogenated graphite led to the destabilization of $LiBH_4$ resulting in complete decomposition of $LiBH_4$ below 400 °C; over 100 °C lower than pure $LiBH_4$ rendering the composite a more viable option for on board storage than pure $LiBH_4$.

The composites potential as a reversible storage medium was also indicated however the recombination conditions need to be investigated and be suitably achievable for the graphite+$LiBH_4$ to be considered a suitable candidate as a future hydrogen storage material. The presence of Li_2C_2 in the dehydrided sample hints that the composite may be reversible over multiple cycles.

7 Conclusion

Graphite was ball-milled for 8 h under 3 bar H_2 before $LiBH_4$ was added at a ratio of 2:1 (Graphite:$LiBH_4$) and milled for a further 2 h. Room temperature XRD and Raman measurements showed that the graphite lattice had been deformed, resulting in the formation of nanocrystalline and amorphous graphite and lithium borohydride. The absence of any new phases indicated no reaction had taken place between graphite and lithium borohydride during milling. No contamination from milling media was observed.

Four reactions were observed upon heating graphite+$LiBH_4$ to 500 °C. These are attributed to the orthorhombic to hexagonal phase change (116 °C), melting (280 °C) and a two-step decomposition reaction all (350 °C) of which originate from $LiBH_4$. The two step decomposition process occurs between 308 °C and 397 °C with the evolution of hydrogen; no methane was detected.

Application of a hydrogen over pressure was shown to influence the decomposition process. A 3 bar H_2 over pressure delayed $LiBH_4$ decomposition by over 100 °C compared to Ar. Hydrogen pressures of 50 bar and 100 bar resulted in the suppression of lithium borohydride decomposition; indicating that under these pressures the system might be reversible.

In-situ measurements were performed to gain an understanding of the decomposition pathway(s) taken during heating. The presence of oxygen during the dehydrogenation process of graphite+$LiBH_4$ affected the decomposition pathway observed, yielding LiO, Li_3BO_3 and $Li_4B_2O_5$. The observed formation of Li_2C_2 showed that the decomposition of a portion of the sample was not affected by oxidation; indicating the possibility for a reversible system based on the mechanism described by Ichikawa et al. [39].

Rehydrogenation was achieved by heating a decomposed sample under 100 bar H_2 to 500 °C at 2 °Cmin^{-1} and held isothermally for 20 min. These conditions resulted in recombination of around 18% of the theoretical total possible, for the $LiBH_4$. It is believed that kinetic limitation prevented complete recombination and that greater uptake would be observed if longer times were used.

The potential of the graphite+$LiBH_4$ composite has been discussed and whilst the reduction in hydrogen desorption temperature and the possibility of reversible cycling are a steps in the right direction, it was concluded that the temperatures and pressures required for the dehydriding and rehydriding processes are too high for practical on-board applications. More research is needed to understand and evaluate the composites reversibility potential.

8 Future Work

Whilst this work shows that the graphite+$LiBH_4$ system holds the potential to be a reversible hydrogen storage system further investigation is required.

It has not been possible to specifically identify the exact origin of the hydrogen evolution from the system and this would be necessary to fully understand the decomposition mechanism. This could be though isotopic exchange (D for H) within the $LiBH_4$ ($LiBD_4$) to determine if any hydrogen is released from the graphite.

$LiBH_4$ is known to substitute hydrogen ions from the gas phase during elevated temperatures [58]. This mechanism may be occurring during high pressure measurements and the origin of the suppression of decomposition and potential recombination. Again isotopic exchanged $LiBD_4$ and high pressure, high temperature in situ Raman spectroscopy would allow further investigation.

Oxygen free in-situ diffraction measurements would allow observation of the crystalline phases and the change in lattice parameters with changing temperature (and atmosphere). Unfortunately the work carried out during this project was subject to unknown oxidation. The source of this oxidization should be eliminated and the measurements performed again.

Finally a more detailed study into reversibility should be performed, to ascertain the fully capacity of reversibility and the conditions needed to achieve this.

9 References

1. Schlapbach, L. and A. Zuttel, *Hydrogen-storage materials for mobile applications.* Nature, 2001. **414**(6861): p. 353-358.
2. *DoE Targets for On-Board Hydrogen Storage Systems for Light-Duty Vehicles*. Available from: http://www1.eere.energy.gov/hydrogenandfuelcells/storage/pdfs/targets_onboard_hydro_storage.pdf. [Accessed: 15/03/2012].
3. von Helmolt, R. and U. Eberle, *Fuel cell vehicles: Status 2007.* Journal of Power Sources, 2007. **165**(2): p. 833-843.
4. Dolan, M.D., *Non-Pd BCC alloy membranes for industrial hydrogen separation.* Journal of Membrane Science, 2010. **362**(1–2): p. 12-28.
5. Rapier, R. *Consumer Energy Report (2011) "Highlights of BP's 2011 Statistical Review of World Energy"* Available from: http://www.consumerenergyreport.com/2011/06/23/highlights-of-bps-2011-statistical-review-of-world-energy/. [Accessed: 22/03/2012].
6. Kothari, R., D. Buddhi, and R.L. Sawhney, *Comparison of environmental and economic aspects of various hydrogen production methods.* Renewable and Sustainable Energy Reviews, 2008. **12**(2): p. 553-563.
7. FSEC. *Hydrogen Basics- Liquid Storage*. Available from: http://www.fsec.ucf.edu/en/consumer/hydrogen/basics/storage-liquid.htm. [Accessed: 11/09/2012].
8. Züttel, A., *Materials for hydrogen storage.* Materials Today, 2003. **6**(9): p. 24-33.
9. Parker, S.F., *Spectroscopy and bonding in ternary metal hydride complexes—Potential hydrogen storage media.* Coordination Chemistry Reviews, 2010. **254**(3–4): p. 215-234.
10. Nijkamp, M.G., J.E.M.J. Raaymakers, A.J. van Dillen, and K.P. de Jong, *Hydrogen storage using physisorption – materials demands.* Applied Physics A: Materials Science & Processing, 2001. **72**(5): p. 619-623.
11. Reed, D. and D. Book, *Recent applications of Raman spectroscopy to the study of complex hydrides for hydrogen storage.* Current Opinion in Solid State and Materials Science, 2011. **15**(2): p. 62-72.
12. Dillon, A.C., K.M. Jones, T.A. Bekkedahl, C.H. Kiang, D.S. Bethune, and M.J. Heben, *Storage of hydrogen in single-walled carbon nanotubes.* Nature, 1997. **386**(6623): p. 377-379.
13. Nix, R. *PE Curves & Energetics of Adsorption*. Available from: http://www.chem.qmul.ac.uk/surfaces/scc/scat2_4.htm. [Accessed: 27/07/2012].
14. Züttel, A. and A. Borgschulte, in *International Symposium on H2 Energy*. 2007: Richmond, USA.
15. Hirscher, M. *Presentation*. in *MH 2004*.
16. Smith, C.I., H. Miyaoka, T. Ichikawa, M.O. Jones, J. Harmer, W. Ishida, P.P. Edwards, Y. Kojima, and H. Fuji, *Electron Spin Resonance Investigation of Hydrogen Absorption in Ball-Milled Graphite.* Journal of Physical Chemistry C, 2009. **113**(14): p. 5409-5416.
17. Fukunaga, T., K. Nagano, U. Mizutani, H. Wakayama, and Y. Fukushima, *Structural change of graphite subjected to mechanical milling.* Journal of Non-Crystalline Solids, 1998. **232–234**(0): p. 416-420.
18. Chen, Y., J. Fitz Gerald, L.T. Chadderton, and L. Chaffron, *Nanoporous carbon produced by ball milling.* Applied Physics Letters, 1999. **74**(19): p. 2782-2784.

19. Haasz, A.A., P. Franzen, J.W. Davis, S. Chiu, and C.S. Pitcher, *Two-region model for hydrogen trapping in and release from graphite.* Journal of Applied Physics, 1995. **77**(1): p. 66-86.
20. Atsumi, H., M. Iseki, and T. Shikama, *Hydrogen behavior in carbon-based materials and its neutron irradiation effect.* Journal of Nuclear Materials, 1996. **233–237, Part 2**(0): p. 1128-1132.
21. Orimo, S., G. Majer, T. Fukunaga, A. Zuttel, L. Schlapbach, and H. Fujii, *Hydrogen in the mechanically prepared nanostructured graphite.* Applied Physics Letters, 1999. **75**(20): p. 3093-3095.
22. Zhang, Y., V.S.J. Mann, D. Reed, A. Walton, I.R. Harris, and D. Book, *Hydrogen storage properties of nanostructured graphite-based materials*. 2009 International Conference on Sustainable Power Generation and Supply, Vols 1-4. 2009, New York: Ieee. 1987-1990.
23. Welham, N.J., V. Berbenni, and P.G. Chapman, *Effect of extended ball milling on graphite.* Journal of Alloys and Compounds, 2003. **349**(1–2): p. 255-263.
24. Zhang, Y. and D. Book, *Effect of Milling Conditions on the Purity of Hydrogen Desorbed from Ball-milled Graphite.* The Journal of Physical Chemistry C, 2011. **115**(51): p. 25285-25289.
25. Pimenta, M., G. Dresselhaus, M.S. Dresselhaus, L. Cancado, A. Jorio, and R. Saito, *Studying disorder in graphite-based systems by Raman spectroscopy.* Physical Chemistry Chemical Physics, 2007. **9**(11): p. 1276-1290.
26. Chen, D.M., T. Ichikawa, H. Fujii, N. Ogita, M. Udagawa, Y. Kitano, and E. Tanabe, *Unusual hydrogen absorption properties in graphite mechanically milled under various hydrogen pressures up to 6 MPa.* Journal of Alloys and Compounds, 2003. **354**(1-2): p. L5-L9.
27. Huang, Z., A. Calka, and H. Liu, *Effects of milling conditions on hydrogen storage properties of graphite.* Journal of Materials Science, 2007. **42**(14): p. 5437-5441.
28. Francke, M., H. Hermann, R. Wenzel, G. Seifert, and K. Wetzig, *Modification of carbon nanostructures by high energy ball-milling under argon and hydrogen atmosphere.* Carbon, 2005. **43**(6): p. 1204-1212.
29. Miyaoka, H., W. Ishida, T. Ichikawa, and Y. Kojima, *Synthesis and characterization of lithium-carbon compounds for hydrogen storage.* Journal of Alloys and Compounds, 2011. **509**(3): p. 719-723.
30. Ichikawa, T., D.M. Chen, S. Isobe, E. Gomibuchi, and H. Fujii, *Hydrogen storage properties on mechanically milled graphite.* Materials Science and Engineering: B, 2004. **108**(1–2): p. 138-142.
31. Zhang, Y. and D. Book, *Hydrogen storage properties of ball-milled graphite with 0.5 wt% Fe.* International Journal of Energy Research, 2011.
32. Hirscher, M., M. Becher, M. Haluska, F. von Zeppelin, X. Chen, U. Dettlaff-Weglikowska, and S. Roth, *Are carbon nanostructures an efficient hydrogen storage medium?* Journal of Alloys and Compounds, 2003. **356–357**(0): p. 433-437.
33. Kiyobayashi, T., H.T. Takeshita, H. Tanaka, N. Takeichi, A. Züttel, L. Schlapbach, and N. Kuriyama, *Hydrogen adsorption in carbonaceous materials–: How to determine the storage capacity accurately.* Journal of Alloys and Compounds, 2002. **330–332**(0): p. 666-669.
34. Kajiura, H., S. Tsutsui, K. Kadono, M. Kakuta, M. Ata, and Y. Murakami, *Hydrogen storage capacity of commercially available carbon materials at room temperature.* Applied Physics Letters, 2003. **82**(7): p. 1105-1107.
35. Takagi, H., H. Hatori, Y. Soneda, N. Yoshizawa, and Y. Yamada, *Adsorptive hydrogen storage in carbon and porous materials.* Materials Science and Engineering: B, 2004. **108**(1–2): p. 143-147.
36. Isobe, S., T. Ichikawa, J.I. Gottwald, E. Gomibuchi, and H. Fujii, *Catalytic effect of 3d transition metals on hydrogen storage properties in mechanically milled graphite.* Journal of Physics and Chemistry of Solids, 2004. **65**(2–3): p. 535-539.

37. Miyaoka, H., T. Ichikawa, T. Fujii, W. Ishida, S. Isobe, H. Fuji, and Y. Kojima, *Anomalous hydrogen absorption on non-stoichiometric iron-carbon compound.* Journal of Alloys and Compounds, 2010. **507**(2): p. 547-550.
38. Ichikawa, T.I., S. Fujii, H., *Hydrogen desorption properties of lithium-carbon-hydrogen system*. Vol. 46. 2005, Sendai, JAPON: Japan Institute of Metals. 3.
39. Ichikawa, T.M., H; Kojima, Y, *Hydrogen Storage Properties of Hydrogenated Graphite and Lithium Hydride Nanocomposite*, in *Advances in Diverse Industrial Applications of Nanocomposites*, B. Reddy, Editor. 2011, InTech. p. 550.
40. Miyaoka, H., T. Ichikawa, and Y. Kojima, *The reaction process of hydrogen absorption and desorption on the nanocomposite of hydrogenated graphite and lithium hydride.* Nanotechnology, 2009. **20**(20): p. 204021.
41. Orimo, S., Y. Nakamori, G. Kitahara, K. Miwa, N. Ohba, S. Towata, and A. Züttel, *Dehydriding and rehydriding reactions of LiBH4.* Journal of Alloys and Compounds, 2005. **404–406**(0): p. 427-430.
42. Reed, D.B., D *In-situ Raman study of the thermal decomposition of LiBH4.* Materials Resource Society Proceedings, 2009. **1216**.
43. Vajo, J.J., T.T. Salguero, A.F. Gross, S.L. Skeith, and G.L. Olson, *Thermodynamic destabilization and reaction kinetics in light metal hydride systems.* Journal of Alloys and Compounds, 2007. **446–447**(0): p. 409-414.
44. Vajo, J.J. and G.L. Olson, *Hydrogen storage in destabilized chemical systems.* Scripta Materialia, 2007. **56**(10): p. 829-834.
45. Yan, Y., A. Remhof, S.-J. Hwang, H.-W. Li, P. Mauron, S.-i. Orimo, and A. Züttel, *Pressure and temperature dependence of the decomposition pathway of LiBH4.* Physical Chemistry Chemical Physics, 2012. **14**(18): p. 6514-6519.
46. Orimo, S.-I., Y. Nakamori, N. Ohba, K. Miwa, M. Aoki, S.-i. Towata, and A. Zuttel, *Experimental studies on intermediate compound of LiBH4.* Applied Physics Letters, 2006. **89**(2): p. 021920-021920-3.
47. Hwang, S.-J., R.C. Bowman, J.W. Reiter, Rijssenbeek, G.L. Soloveichik, J.-C. Zhao, H. Kabbour, and C.C. Ahn, *NMR Confirmation for Formation of [B12H12]2- Complexes during Hydrogen Desorption from Metal Borohydrides.* The Journal of Physical Chemistry C, 2008. **112**(9): p. 3164-3169.
48. Kato, S., M. Bielmann, A. Borgschulte, V. Zakaznova-Herzog, A. Remhof, S.-i. Orimo, and A. Zuttel, *Effect of the surface oxidation of LiBH4 on the hydrogen desorption mechanism.* Physical Chemistry Chemical Physics, 2010. **12**(36): p. 10950-10955.
49. Cahen, S., J.B. Eymery, R. Janot, and J.M. Tarascon, *Improvement of the LiBH4 hydrogen desorption by inclusion into mesoporous carbons.* Journal of Power Sources, 2009. **189**(2): p. 902-908.
50. Rahmat, N., A.Z. Abdullah, and A.R. Mohamed, *A Review: Mesoporous Santa Barbara Amorphous-15, Types, Synthesis and Its Applications towards Biorefinery Production.* American Journal of Applied Sciences, 2010. **7**(12): p. 1579-1586.
51. Baerns, M., *Basic Principles in Applied Catalysis*. 2010: Springer.
52. Zhang, Y., W.-S. Zhang, A.-Q. Wang, S. Li-Xian, M.-Q. Fan, H.-L. Chu, J.-C. Sun, and T. Zhang, *LiBH4 nanoparticles supported by disordered mesoporous carbon: Hydrogen storage performances and destabilization mechanisms.* INTERNATIONAL JOURNAL OF HYDROGEN ENERGY, 2007. **32**(16): p. 3976-3980.
53. Zhang, Y., A. Bevan, and D. Book, *Hydrogen desorption behaviour of a ball-milled graphite - LiBH4 composite.* MRS Online Proceedings Library, 2012. **1386**.
54. Available from: http://www.retsch.com/products/milling/planetary-ball-mills/pm-400/. [Accessed: 03/05/2012].

55. Pendolino, F., P. Mauron, A. Borgschulte, and A. Züttel, *Effect of Boron on the Activation Energy of the Decomposition of LiBH4.* The Journal of Physical Chemistry C, 2009. **113**(39): p. 17231-17234.
56. Züttel, A., P. Wenger, S. Rentsch, P. Sudan, P. Mauron, and C. Emmenegger, *LiBH4 a new hydrogen storage material.* Journal of Power Sources, 2003. **118**(1–2): p. 1-7.
57. Morgan, W.C., *Thermal expansion coefficients of graphite crystals.* Carbon, 1972. **10**(1): p. 73-79.
58. Borgschulte, A., R. Gremaud, Z. Lodziana, and A. Zuttel, *Hydrogen tracer diffusion in LiBH4 measured by spatially resolved Raman spectroscopy.* Physical Chemistry Chemical Physics, 2010. **12**(19): p. 5061-5066.